01 Jan 2016

Deployment And Performance Analyses Of High-resolution Iowa XPOL Radar System During The NASA IFloodS Campaign

Kumar Vijay Mishra

Witold F. Krajewski

Radoslaw Goska

Daniel Ceynar

et. al. For a complete list of authors, see https://scholarsmine.mst.edu/civarc_enveng_facwork/2649

Recommended Citation

K. V. Mishra and W. F. Krajewski and R. Goska and D. Ceynar and B. C. Seo and A. Kruger and J. J. Niemeier and M. B. Galvez and M. Thurai and V. N. Bringi and L. Tolstoy and P. A. Kucera and W. A. Petersen and J. Grazioli, "Deployment And Performance Analyses Of High-resolution Iowa XPOL Radar System During The NASA IFloodS Campaign," *Journal of Hydrometeorology*, vol. 17, no. 2, pp. 455 - 479, American Meteorological Society, Jan 2016.
The definitive version is available at https://doi.org/10.1175/JHM-D-15-0029.1

SPECIAL
IFloodS
COLLECTION

Deployment and Performance Analyses of High-Resolution Iowa XPOL Radar System during the NASA IFloodS Campaign

KUMAR VIJAY MISHRA,[*,+,#,@] WITOLD F. KRAJEWSKI,[*,+,&] RADOSLAW GOSKA,[*,+] DANIEL CEYNAR,[*,+] BONG-CHUL SEO,[*,+] ANTON KRUGER,[*,+,#] JAMES J. NIEMEIER,[*,+] MIGUEL B. GALVEZ,[**] MERHALA THURAI,[**] V. N. BRINGI,[**] LEONID TOLSTOY,[**] PAUL A. KUCERA,[++] WALTER A. PETERSEN,[##] JACOPO GRAZIOLI,[@@] AND ANDREW L. PAZMANY[&&]

[*] *Iowa Flood Center, The University of Iowa, Iowa City, Iowa*
[+] *IIHR–Hydroscience and Engineering, The University of Iowa, Iowa City, Iowa*
[#] *Department of Electrical and Computer Engineering, The University of Iowa, Iowa City, Iowa*
[@] *Department of Mathematics, The University of Iowa, Iowa City, Iowa*
[&] *Department of Civil and Environmental Engineering, The University of Iowa, Iowa City, Iowa*
[**] *Department of Electrical and Computer Engineering, Colorado State University, Fort Collins, Colorado*
[++] *Research Applications Laboratory, National Center for Atmospheric Research, Boulder, Colorado*
[##] *Wallops Flight Facility, NASA Goddard Space Flight Center, Wallops Island, Virginia*
[@@] *Environmental Remote Sensing Laboratory (LTE), École Polytechnique Fédérale de Lausanne, Lausanne, Switzerland*
[&&] *ProSensing Inc., Amherst, Massachusetts*

(Manuscript received 5 February 2015, in final form 24 August 2015)

ABSTRACT

This article presents the data collected and analyzed using the University of Iowa's X-band polarimetric (XPOL) radars that were part of the spring 2013 hydrology-oriented Iowa Flood Studies (IFloodS) field campaign, sponsored by NASA's Global Precipitation Measurement (GPM) Ground Validation (GV) program. The four mobile radars have full scanning capabilities that provide quantitative estimation of the rainfall at high temporal and spatial resolutions over experimental watersheds. IFloodS was the first extensive test of the XPOL radars, and the XPOL radars demonstrated their field worthiness during this campaign with 46 days of nearly uninterrupted, remotely monitored, and controlled operations. This paper presents detailed postcampaign analyses of the high-resolution, research-quality data that the XPOL radars collected. The XPOL dual-polarimetric products and rainfall are compared with data from other instruments for selected diverse meteorological events at high spatiotemporal resolutions from unprecedentedly unique and vast data generated during IFloodS operations. The XPOL data exhibit a detailed, complex structure of precipitation viewed at multiple range resolutions (75 and 30 m). The inter-XPOL comparisons within an overlapping scanned domain demonstrate consistency across different XPOL units. The XPOLs employed a series of heterogeneous scans and obtained estimates of the meteorological echoes up to a range oversampling of 7.5 m. A finer-resolution (30 m) algorithm is described to correct the polarimetric estimates for attenuation at the X band and obtain agreement of attenuation-corrected products with disdrometers and NASA S-band polarimetric (NPOL) radar. The paper includes hardware characterization of Iowa XPOL radars conducted prior to the deployment in IFloodS following the GPM calibration protocol.

1. Introduction

It is widely accepted that precipitation monitoring is difficult because of its high spatial and temporal variability (see, e.g., Wilson and Brandes 1979; Zawadzki 1982; Krajewski and Smith 2002); nonetheless, rainfall remains one of the most critical variables in many hydrological applications (Battan 1973; Chow et al. 1988). A number of studies and experiments have used rain gauges and disdrometers to establish the spatiotemporal variability of rainfall with direct in situ measurements (Ciach and Krajewski 1999a,b);

Corresponding author address: Kumar Vijay Mishra, IIHR–Hydroscience and Engineering, The University of Iowa, 100 Stanley Hydraulics Laboratory, Iowa City, IA 52242.
E-mail: kumarvijay-mishra@uiowa.edu

Publisher's Note: This article was revised on 28 January 2016 to correct a line of text in section 7, p. 471, which was inaccurate when originally published.

DOI: 10.1175/JHM-D-15-0029.1

a detailed exposition of these ground-based methods can be found in Habib et al. (2010). However, these instruments do not yield precipitation measurements in the space–time continuum. On the other hand, while the wide use of modern weather radar systems has enabled continuous rainfall measurements in the space–time domain (Doviak and Zrnić 1993; Bringi and Chandrasekar 2001; Bringi et al. 2007), this feature compromises the accuracy of the radar rainfall products when compared with the in situ estimates (see, e.g., Krajewski et al. 1996; Seo and Smith 1996; Smith et al. 1996; Gebremichael and Krajewski 2004; Tabary 2007). We refer the reader to Villarini and Krajewski (2010) for an exhaustive review of the uncertainties in radar rainfall estimates.

High-resolution, fast-scanning radars should be deployed to combat the differences in spatiotemporal resolutions of radar and rain gauge sampling regimes. However, the sampling geometry, resolution, and temporal coverage of the conventional S- and C-band weather radars, which constitute many national weather radar networks (Klazura and Imy 1993; Lapczak et al. 1999; Gekat et al. 2004), are designed primarily to observe mesoscale weather phenomena. Further, popular NEXRAD rainfall estimates are available at ~1–4 km^2 resolution (Lin and Mitchell 2005; Zhang et al. 2011), while there is evidence that rainfall variability is significant below this resolution (Krajewski et al. 2003). More importantly, detailed observations of rainfall at the near-ground level remain undetected in S- and C-band radars at far ranges because of the sparsity of the operational networks. Therefore, it has become increasingly more common to use shorter wavelengths, such as those in the X and Ku bands, to complement the S- and C-band rainfall observations and monitor the precipitation variability at scales smaller (e.g., basin) than the available products from the longer-wavelength radars (see, e.g., McLaughlin et al. 2009; Maki et al. 2010; Yoshikawa et al. 2010).

Employing a network of several identical units often compensates for X-band radars' lack of spatial coverage. This strategy has proved economically and operationally feasible, as demonstrated by X-band networks such as those used by the Collaborative Adaptive Sensing of the Atmosphere (CASA) Integrated Project 1 (IP1; McLaughlin et al. 2009), X-Band Polarimetric Radar Information (X-RAIN; Maki et al. 2010), and the Tropical Radar Network (TropiNet; Galvez et al. 2009). The objective of these X-band weather radar networks is to retrieve meteorological echoes in the lower troposphere and to adapt to rapidly changing severe weather. The hydrological quest (Krajewski et al. 2010) to finely resolve rainfall in space and time remains secondary to the stated objectives of such X-band networks. Therefore, the research in hydrology would benefit from an X-band weather radar network that focuses exclusively on the hydrological aspects of radar rainfall estimation such as flood prediction or soil erosion.

With the objective of conducting hydrology-focused research and obtaining accurate quantitative estimation of rainfall at a high temporal and spatial resolution, the University of Iowa has acquired four scanning, mobile, X-band polarimetric (XPOL) Doppler weather radars. The four Iowa radars are designated as XPOL-2, XPOL-3, XPOL-4 and XPOL-5 [XPOL-1 is the unit described in Schneebeli et al. (2013)]. Iowa procured these XPOL radars from ProSensing under the Major Research Instrumentation (MRI) grant funded by the National Science Foundation (NSF). The Iowa XPOL system's distinct engineering and operational abilities facilitate the study of near-ground hydrological processes at smaller scales. Several of the XPOL radar system's features make it more appealing to the hydrology community than the existing networks of X-band weather radars. First, while many existing X-band weather radars are installed on tower tops, the Iowa XPOL radars are mounted on mobile platforms. Consequently, Iowa XPOL radars are more versatile and can be deployed in various regions to provide high-resolution radar observations of precipitation. Iowa XPOL radars can also provide high-resolution, near-surface observations for those basins that might be located far from the existing NEXRADs. Second, because XPOL systems can acquire data at a programmable range oversampling, which can be as low as 7.5 m, they provide more accurate polarimetric estimates without decreasing the scan rate (Torres and Zrnić 2003). Third, unlike existing X-band networks, the Iowa XPOL network provides very high-resolution precipitation vertical profiles of up to 15-m range resolution. In a previous study, Schneebeli et al. (2013) used an X-band radar unit similar to the Iowa XPOL radars to observe high-resolution vertical profiles in the Swiss Alps region. The Iowa XPOL radars can facilitate similar studies for snow-to-rain transition regions. When used as a network, the radars can capture multiple high-resolution snapshots of the same storm from different angles. The radars are intended to serve multiple areas of hydrological research, including uncertainty modeling, urban hydrology, flood and flash-flood prediction, and soil erosion.

In this paper, we present the first data and analyses of the Iowa XPOL radars' high-resolution observations during their maiden field deployment. We provide a novel perspective on precipitation estimates by introducing the high-resolution observations at near-ground levels by mobile X-band radars. As explained in the next section, previous studies have documented precipitation observations at coarse spatiotemporal resolutions and use tower-top-mounted X-band networks. Our analyses indicate that the high-resolution XPOL observations agree

well with the in situ ground instruments and provide more detailed features of storms not captured by the S-band radar. We describe the salient features of the Iowa XPOL radars and their scientific objectives in section 2 and compare them with existing X-band radars. Section 3 gives a brief overview of the field campaign and the deployment of Iowa XPOL radars. Section 4 provides a performance analysis of the raw data and meteorological products, including the range-oversampling capabilities of the Iowa XPOL radars. We introduce the attenuation-correction algorithm for XPOL-4 in section 5. Section 6 demonstrates the consistency of Iowa XPOL data across different radar units. Finally, we compare the meteorological data from XPOL radars with the 2D video disdrometers (2DVDs) and NASA S-band polarimetric (NPOL) radar in section 7. We provide details on XPOL hardware and results from engineering characterization prior to the field campaign in the appendix.

2. Iowa XPOL radars

X-band weather radars have been used for important hydrological studies concerning the spatiotemporal variability of rainfall (see, e.g., Delrieu et al. 1999; Berne and Uijlenhoet 2006; Uijlenhoet and Berne 2008; Scipión et al. 2013). A detailed observational study using an X-band radar operating at a spatial resolution of 120 m and temporal resolution of 16 s can be found in van de Beek et al. (2010). The CASA radars typically operate at range resolutions of 100 or 50 m with a scan rate of $12° s^{-1}$ (McLaughlin et al. 2009). Similarly, mobile X-band radars such as Agenzia Regionale per la Protezione Ambientale (ARPA) Piemonte (ARX), operating at a range resolution of 125 m and a beamwidth of 1.3°, have previously been used (Cremonini et al. 2010). During the early 1990s, Fabry et al. (1992) carried out various experiments using a mobile X-band vertically pointing radar (VPR) to obtain high-resolution (20 m) data for stratiform events. Similarly, Purdy et al. (2005) made high-resolution (60 m) hydrological measurements using a mobile X-band VPR during the Southern Alps Experiment (SALPEX) in New Zealand to understand a complex precipitation process such as the seeder–feeder mechanism. Kabeche et al. (2010) have analyzed quantitative precipitation estimates obtained from a network of X-band radars operating at 300 m. Pazmany et al. (2013) have deployed a mobile X-band radar that employs a traveling wave tube amplifier (TWTA) to study severe storms and tornadoes at a minimum range resolution of 15 m and azimuthal scan rates of $180° s^{-1}$. Picciotti et al. (2013) reported hydrologic applications with a network of three low-power X-band dual-polarization radars in Moldova at 250-m range resolution. Borque et al. (2014) have also actively used an X-band network to assist in cloud radar studies. Compared to these existing applications, the mobile Iowa XPOL radars push the range resolutions at 3-cm regimes to smaller scales, on the order of 15 m, enabling detection of detailed precipitation structures at finer scales with an acceptable accuracy. While the cross-beam resolution clearly remains limited here, the flexibility in deployment and operation of each of these low-cost XPOL units aids in achieving our research goals that we briefly describe in the following subsection.

a. Scientific objectives

As previously discussed, while conventional lower-frequency (S and C band) weather radar data are limited to 100–300-m range resolution, the Iowa XPOL system can provide radar rainfall data at higher-range resolutions. Further, the radars are configured to observe target-of-opportunity storms from multiple look angles within narrow high spatiotemporal windows. Such observations of the same precipitation event with several radars can mitigate signal attenuation due to precipitation at the X band (Krajewski 2007). The Iowa XPOL data can be used to model the spatial dependence of the errors at smaller scales, which is useful when constructing input for ensemble-based predictive models. Another key scientific goal is to understand the scaling behavior of rainfall below the scale of about 1 km, which Fabry et al. (1992) documented in earlier studies using a VPR capable of making measurements up to 7.5 m. Eventually, the fully operational XPOL radars are expected to aid in more elaborate applications of urban hydrology and flash-flood prediction.

Our specific goals for this paper are more modest. We demonstrate 1) the advantage of having two X-band radars versus just one in combating the attenuation problem, 2) good agreement between the radar observables and disdrometer-based data, and 3) the ability of our radars to provide meaningful data at very high spatial resolution. This demonstration is necessary prior to any future analysis of the Iowa Flood Studies (IFloodS) data and their hydrologic applications. Studies published to date (Cunha et al. 2015; Seo et al. 2015) show that NEXRAD-based products suffer significant problems for some events and XPOL data; the placement of the radars can help illuminate some of the causes, but this is outside of the scope of this paper.

b. Technical specifications

Table 1 lists the salient technical parameters of the Iowa XPOL radars. Each of the Iowa XPOL radars is deployed on a flatbed-trailer-mounted system and is capable of taking measurements at remote and secure locations where power and Internet facilities are available. The trailer platform enables the use of a parabolic

TABLE 1. Technical specifications of a typical unit in the Iowa XPOL radar system.

Technical characteristic	Description
System	
Nominal R_{max}	40 km
Range resolution	Selectable 15–150 m
Sensitivity	−5 dBZ at 10 km at range resolution of 75 m
Mounting platform	8 ft × 10 ft customized trailer
Power supply	On-site and trailer-mounted UPS
Time–location sync source	On-site GPS
Radar and antenna controller	Remote operated web interface
Antenna	
Shape	Parabolic
Polarization	Dual polarized
Diameter	6 ft
Gain	42 dBi
3-dB beamwidth	1.3°–1.5°
Cross-polarization isolation	~30 dB
Max voltage standing wave ratio	~1.25
Scanning	Azimuth 0°–360°, elevation 0°–90°
Transmitter	
Operating frequency	9.41 GHz
Transmitter	Magnetron, peak power P_t = 25 kW
Pulsing schemes	Staggered PRT and dual PRF
Receiver	
RF receiver gain	~33 dB
Cross-channel receiver isolation	>50 dB
Noise figure	~3 dB
Dynamic range	80 dB
Digital noise floor	−84 dBm (at 2-MHz receiver bandwidth)
Signal and data processor	
Digital receiver bandwidth	Selectable 2–20 MHz
Range oversampling	Programmable 7.5–75 m
Processing modes	Standard pulse pair, dual pulse pair, and FFT mode
Data products	
Data archiving	On-site on-demand for raw time series and processed products
Archived products	Standard moments: Equivalent reflectivity factor (i.e., Z_h, Z_v), Doppler velocity v and Doppler spectrum width σ_v Dual-polarimetric products: Differential reflectivity (i.e., Z_{dr}), copolar correlation coefficient (i.e., ρ_{hv}), and differential phase (i.e., ψ_{dp}) Derived products: Instantaneous rainfall rate, specific differential phase (i.e., K_{dp})
Available data format	NetCDF

antenna dish that is 6 ft in diameter—slightly larger than the 4 ft dish used in tower-mounted X-band radars (McLaughlin et al. 2009)—leading to enhanced azimuthal resolution. The radars are equipped with an on-site uninterrupted power supply (UPS) and can be controlled and monitored remotely over the Internet. Essentially, each unit is a self-reliant system with an on-site, on-demand archiving capability for raw time series and polarimetric products, global positioning system (GPS)-enabled time and location information, and Internet access to archived data. The transmitter is magnetron based with a peak output power of 25 kW. The radars can operate in staggered pulse repetition time (PRT; Zrnić and Mahapatra 1985) and dual-PRF pulsing modes and can process data using either standard pulse pair or spectral mode techniques. An advanced signal processor computes the polarimetric estimates in multiple modes such as autocovariance and spectral processing (Doviak and Zrnić 1993) at selectable range resolutions and range-oversampling ratios. At the default range resolution of 75 m, the radars have a clear air sensitivity of −5 dBZ at a range of 10 km, which allows the radar to observe light to heavy precipitation up to a maximum unambiguous range R_{max} of 40 km.

3. NASA GPM IFloodS campaign

During April–June 2013, Iowa XPOL radars participated in their first field campaign—Iowa Flood Studies (IFloodS)—which was organized in central and northeastern Iowa in the midwestern United States by

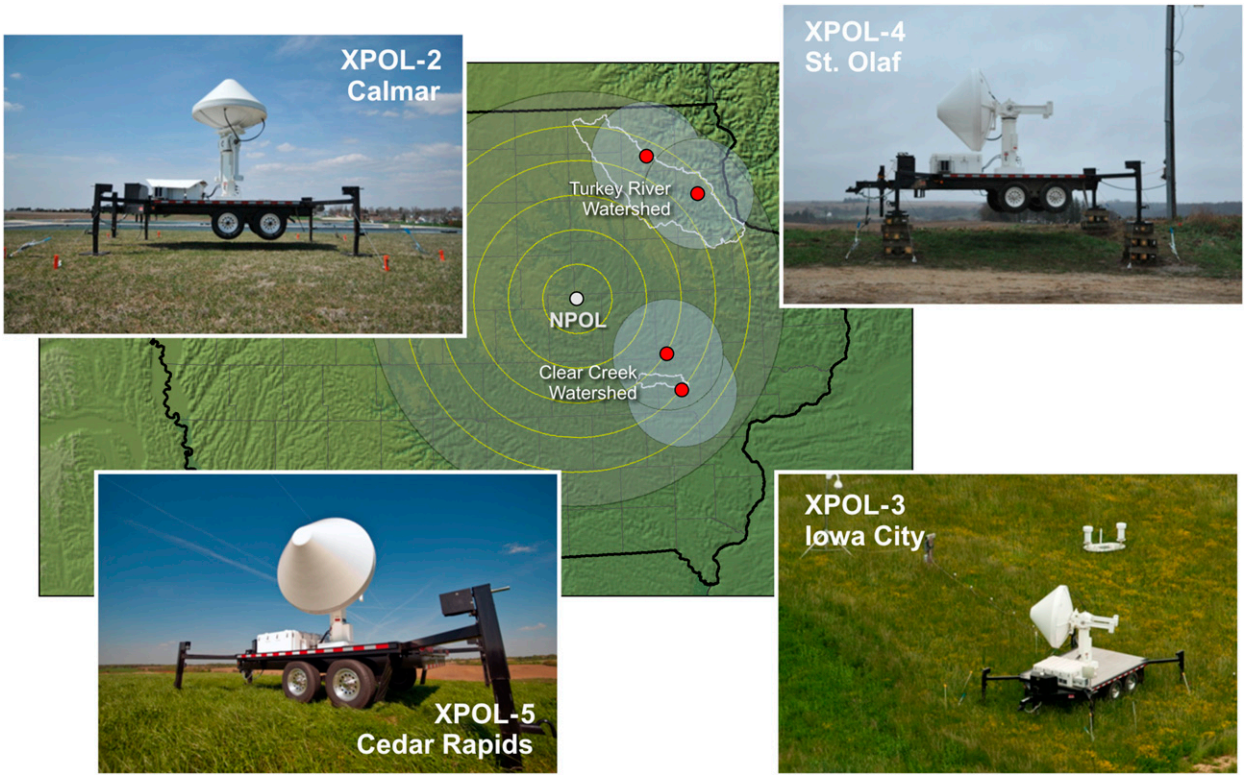

FIG. 1. Deployment locations of the XPOL radars during IFloodS in the far-range regions of the NPOL radar. XPOL-2 and XPOL-4 were deployed at the Calmar and St. Olaf sites with overlapping coverage of the Turkey River watershed (shown in white). Similarly, XPOL-3 and XPOL-5 were deployed at the Iowa City Landfill and Eastern Iowa Airport sites with overlapping coverage of the Clear Creek watershed (shown in white).

NASA in collaboration with the Iowa Flood Center (Petersen and Krajewski 2013). As an important component of the Ground Validation (GV) program of the NASA Global Precipitation Measurement (GPM) satellite mission, IFloodS was one of the first field campaigns dedicated to hydrological studies. We extensively examine the two assumed advantages of the Iowa XPOL units—high spatial resolution and the ability to mitigate attenuation using multiple radars—herein using data collected during IFloodS.

We deployed the XPOL-2 and XPOL-4 units with overlapping coverage over the Turkey River watershed while similarly deploying the XPOL-3 and XPOL-5 units over the Clear Creek watershed (Fig. 1). We intended for the pairwise deployment of XPOL radars to provide useful data in order to cross validate the consistency of near-Earth XPOL observations for the same meteorological events over the watershed.

During IFloodS, XPOL-2 and XPOL-4 units collected data for diverse meteorological events (from light rain to severe storms) with nearly uninterrupted operation for 46 days of the campaign at different spatiotemporal scales (see Fig. 2). The XPOL scan strategy involved a heterogeneous suite of scans for testing various engineering capabilities of the radars and cross validation with other instruments. The radars made polarimetric observations at multiple range resolutions (75 and 30 m) with oversampled range spacings of 75, 30, 15, and 7.5 m. These data were collected at the scan rate of $5^\circ s^{-1}$ in both plan position indicator (PPI) and range–height indicator (RHI) scans. We had enabled the clutter filters in the XPOL signal processors during the IFloodS data collection. Also, we carried out low-elevation surveillance scans to generate a clutter map. Based on these scans, whenever substantial blockage was present in radar coverage, we excluded 1° or 2° elevation scans from the scan strategy for XPOL radars.

Compared to the XPOL-2 and XPOL-4 pair, the data collection of XPOL-3 and XPOL-5 was impaired by frequent shutdown of power and Internet lines. While we primarily analyze interesting datasets corresponding to XPOL-2 and XPOL-4, we also produce data from XPOL-3 and XPOL-5 wherever possible. We emphasize the fact that because all four units are nearly identical, data from any one of them should suffice for demonstration purposes.

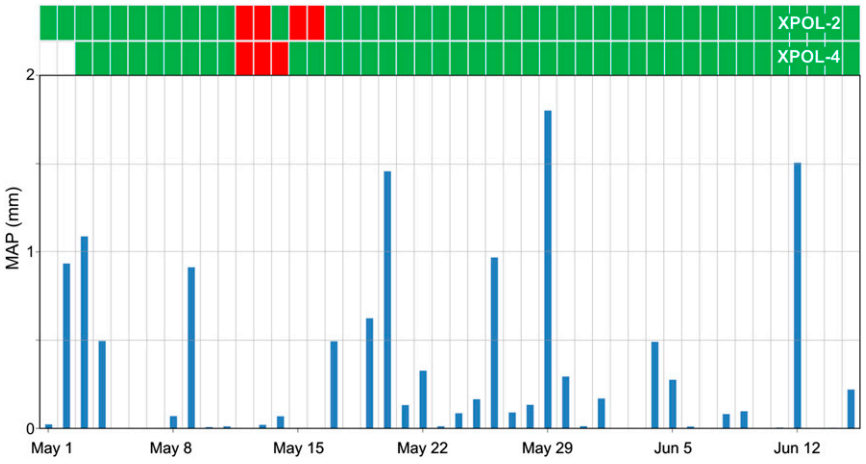

FIG. 2. Deployment and operational statistics for XPOL-2 and XPOL-4 during the IFloodS period (from 1 May to 15 Jun 2013). The blue graph at the bottom represents the daily mean areal precipitation (MAP) for the Turkey River watershed. The top two graphs represent the statuses of XPOL-2 and XPOL-4. The green box indicates that the radar was operational and archiving data. The red box stands for the down-day of the radar. The box is left blank (white) to indicate when the radar was not deployed.

The scan strategy for XPOL radars during IFloodS comprises three scan sets: campaign, surveillance, and safe modes. The campaign-mode scan consisted of a low-elevation surveillance full PPI scan at $5^\circ s^{-1}$, sector PPI scans at $5^\circ s^{-1}$ in the overlapping coverage with the other XPOL radar of the paired configuration (the paired configurations being XPOL-2 and XPOL-4, and XPOL-3 and XPOL-5) in elevations from 2° (or 3°, depending on clutter-map scans) to 8° in increments of 1°, a birdbath (vertically pointing) scan at $12^\circ s^{-1}$, and one RHI each in the direction of the NPOL radar and the other XPOL radar in the pair at $5^\circ s^{-1}$. The default range resolutions of XPOL-2 and XPOL-4 were 75 and 30 m, respectively. The XPOL radars would carry out interleaving scans at finer-range samplings after completing a few sets of campaign-mode scans. For example, the XPOL-2 would perform 10 campaign-mode scans at the default range resolution (and range sampling of 75 m) followed by one campaign-mode scan each at range samplings of 30, 15, and 7.5 m. Similarly, XPOL-4 would scan once in campaign mode for range samplings of 15 and 7.5 m after completing 10 scans at the range sampling of 30 m.

The radars were put on surveillance-mode scans whenever there was precipitation in the IFloodS region but not in the XPOL coverage area. These scans consisted of one low-elevation scan at $5^\circ s^{-1}$ in every 15 min. When a dry day (i.e., no precipitation) was forecast in the IFloodS region, the radars were configured for the safe-mode scan. In this mode, the radars would scan in a vertically pointing position but not record or archive any data.

4. Performance analyses at high spatiotemporal resolutions

The results of the engineering tests (see appendix) established good calibration of the XPOL hardware. In the following subsections, we present stand-alone analysis of the data collected by an XPOL radar through verification of in-phase I and quadrature-phase Q statistics, first high-resolution polarimetric observations of the radar, and validation of experimentally observed sensitivity.

a. *Self-consistency of XPOL data*

On 6 August 2012, that is, almost one year prior to the IFloodS campaign, XPOL-3 collected samples of the received signal in precipitation in fixed-antenna mode at 75-m-range resolution during its test deployment at the Colorado State University–University of Chicago–Illinois State Water Survey (CSU-CHILL) radar facility in Greeley, Colorado. We analyzed these samples to observe their consistency with the respective theoretical distributions. Figures 3 and 4 show the range profiles of horizontal h and vertical v reflectivity products (Z_h and Z_v). Figures 3e and 3f and Figs. 4e and 4f show the histograms of the digitized samples of in-phase and quadrature-phase components of the received signal from a single-range-resolution volume. Each of the I and Q histograms should empirically follow a zero-mean Gaussian distribution (Bringi and Chandrasekar 2001, 287–290), as the received signal is a circular (Fjørtoft and Lopès 2001) or proper (Scherier and Scharf 2010, p. 53) complex Gaussian distribution with zero mean. As

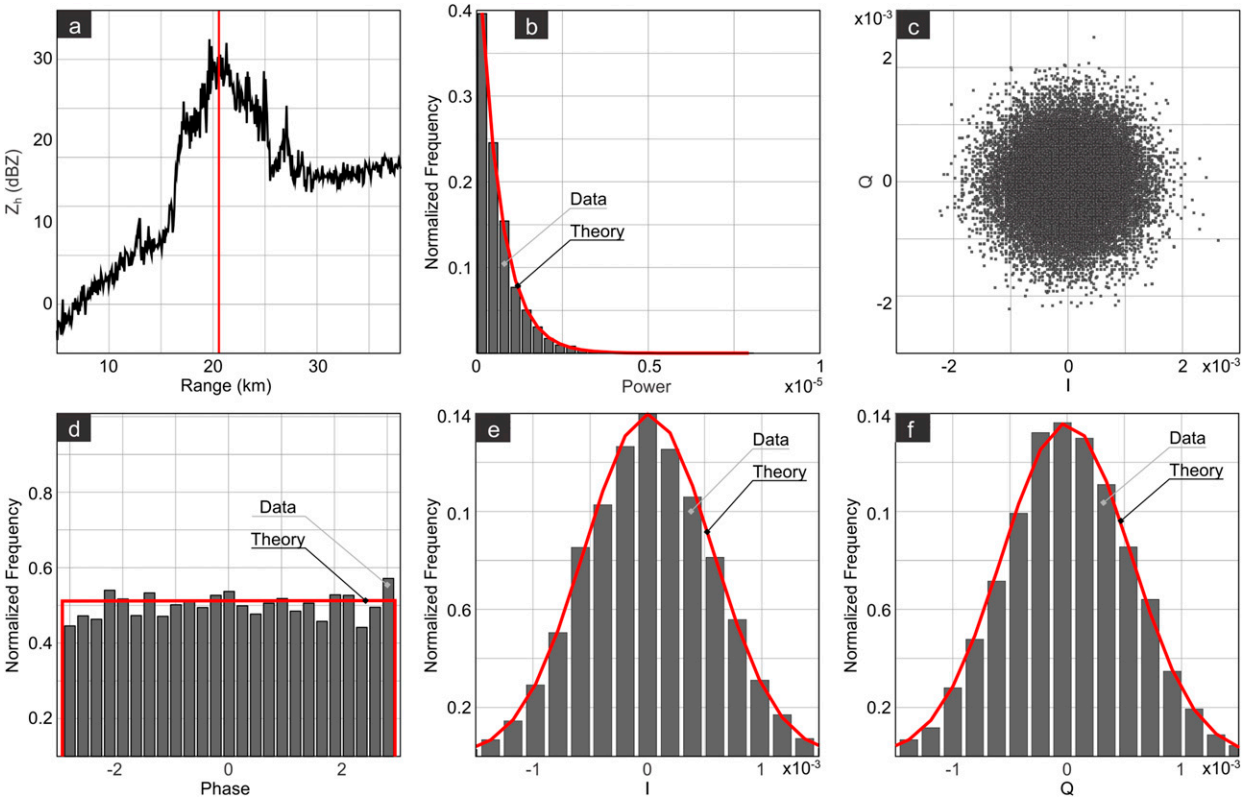

FIG. 3. (a) Range profile of the reflectivity product for the horizontal polarization, as observed by XPOL-3 in a fixed-antenna mode. The red vertical line denotes the range bin for which samples are analyzed in subsequent panels. The in-phase and the quadrature-phase components of the received signal are (c) statistically independent and (e),(f) have a zero-mean Gaussian distribution for the precipitation data with almost identical variances. As expected, the (b) power and (d) phase have exponential and uniform distributions, respectively. The data shown here for a moderate rain event (6 Aug 2012) correspond to the h channel of the XPOL-3 unit that was deployed at the CSU-CHILL site in Greeley, Colorado.

illustrated in Table 2, a Gaussian curve fit on these histograms yields a coefficient of determination R^2 (Draper and Smith 1998), which connotes a more than 99% fit with mean values lying very close to zero. Further, the standard deviations of I and Q samples for a particular polarization are expectedly identical, varying only at a fifth decimal place. Figures 3c and 4c show a scattergram of I versus Q. It can be observed that the scattergram is spread equally in all directions with respect to the origin, implying that the I and Q samples are uncorrelated. Since I and Q samples follow a Gaussian distribution, their uncorrelatedness also implies stochastic independence (Papoulis and Pillai 2002). Figures 3b and 4b show the histogram of the power samples ($I^2 + Q^2$), which, as theorized in Papoulis and Pillai (2002), should be an exponential distribution. Here, an exponential curve fit on the histogram of the power samples yields a fit of 99.867% and 99.957% for horizontal and vertical polarizations, respectively. Figures 3d and 4d show the phase of the received voltage, which follows a uniform distribution, as it should if I and Q are independently Gaussian. Therefore, the distributions of the digitized I and Q samples of the XPOL radars for the precipitation echo are in good agreement with the theory.

b. *Stratiform rain observations at 30-m resolution*

During IFloodS, the XPOL radars made several high-resolution observations of diverse meteorological events in the volume scan mode (stacked sector PPI scans with increasing elevations). Figure 5 shows the three-dimensional structure of a stratiform rain event observed by the XPOL-2 radar at 30-m-range resolution on 12 June 2013. Each horizontal panel shows a different meteorological product for increasing elevations (in steps of 1°) in the azimuthal sector 60°–180°. The entire volume scan mode observation was completed in less than 3 min with the lowest- and highest-elevation scans at 0151 and 0154 UTC, respectively. Starting at an elevation of 4°, the bright band is clearly visible in Figs. 5a and 5e, as noted by the higher values of Z_h and lower values of the copolar correlation coefficient ρ_{hv}, respectively, in the melting layer regions. These observations

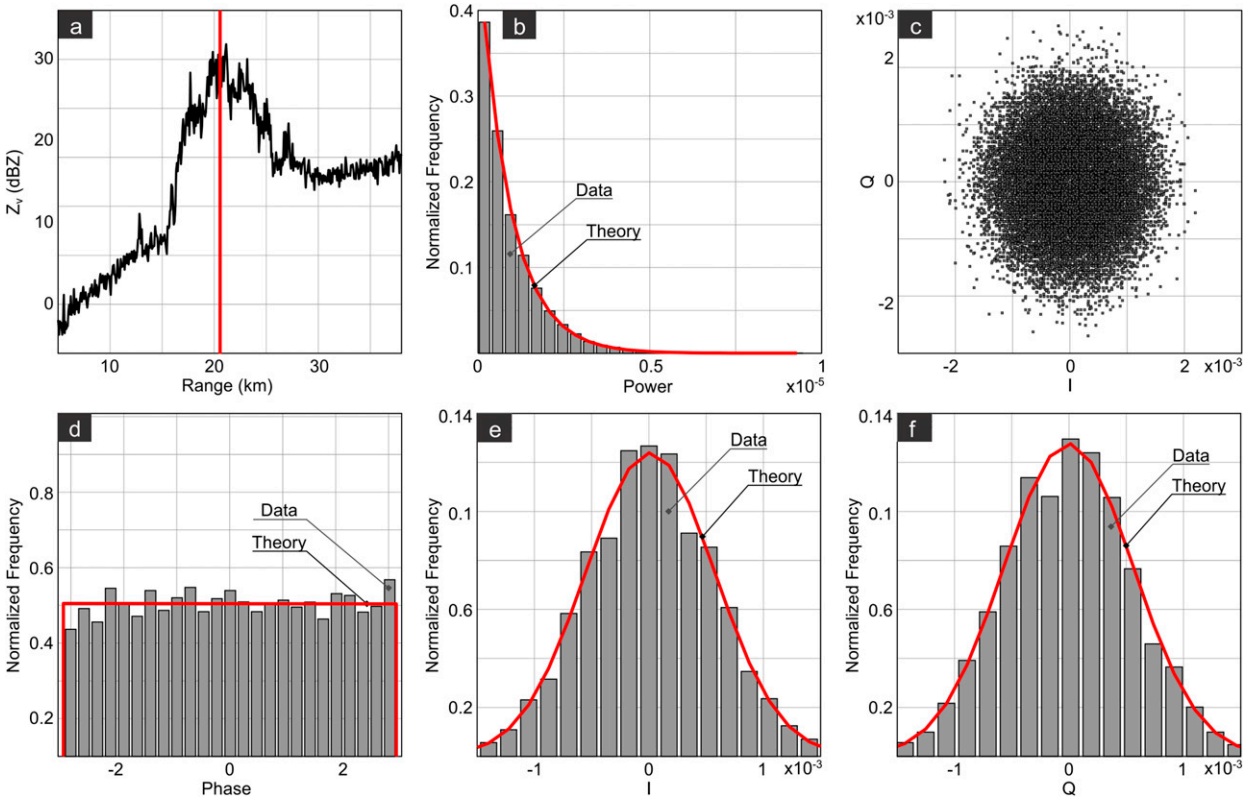

FIG. 4. As in Fig. 3, but for the v channel of the XPOL-3.

demonstrate that Iowa XPOL radars can detect the detailed structure of storms at high spatiotemporal resolutions. The data, as shown here, have not been corrected for attenuation, though the differential reflectivity Z_{dr} has been corrected for any systemwide bias using the nearest (in time) vertical-pointing data for the light rain.

c. *Sensitivity analyses*

The sensitivity of the radar is measured in terms of the minimum detectable reflectivity Z_{min} (dBZ) at a particular range. The Z_{min} is usually defined for the signal-to-noise ratio (SNR) of 0 dB (see Bringi and Chandrasekar 2001, p. 334). From the weather radar equation, the reflectivity (and, consequently, its minimum value) is an inverse function of the range resolution Δr of the radar. A higher value of Z_{min} implies lower sensitivity.

The hydrological goals of the XPOL radars mandate that the radars should be able to detect light rain. However, XPOL radars also participate in a variety of research projects where radars should ideally respond to nonmeteorological scatterers, including insects and birds, refractive index variations, and ground targets. Therefore, as mentioned earlier, the nominal sensitivity of XPOL is specified somewhat lower than the light rain at -5 dBZ when measured at the range resolution of 75 m at the 10-km range. The XPOL radars can be programmed for range resolutions of 150, 105, 75, 30, and 15 m. During IFloodS, most of the XPOL radars operated with the range resolution of 75 m, with

TABLE 2. Statistical properties of the received signal of XPOL-3 data collected during a moderate rain event in Greeley, Colorado, on 6 Aug 2012. Values of I and Q are measured in volts.

	h channel		v channel	
Statistics	I	Q	I	Q
Mean	9.3587×10^{-6}	-4.3502×10^{-6}	10.802×10^{-6}	-3.4486×10^{-6}
Std dev	5.5963×10^{-4}	5.6273×10^{-4}	5.6341×10^{-4}	5.6495×10^{-4}
R^2	0.9950	0.9978	0.9905	0.9910

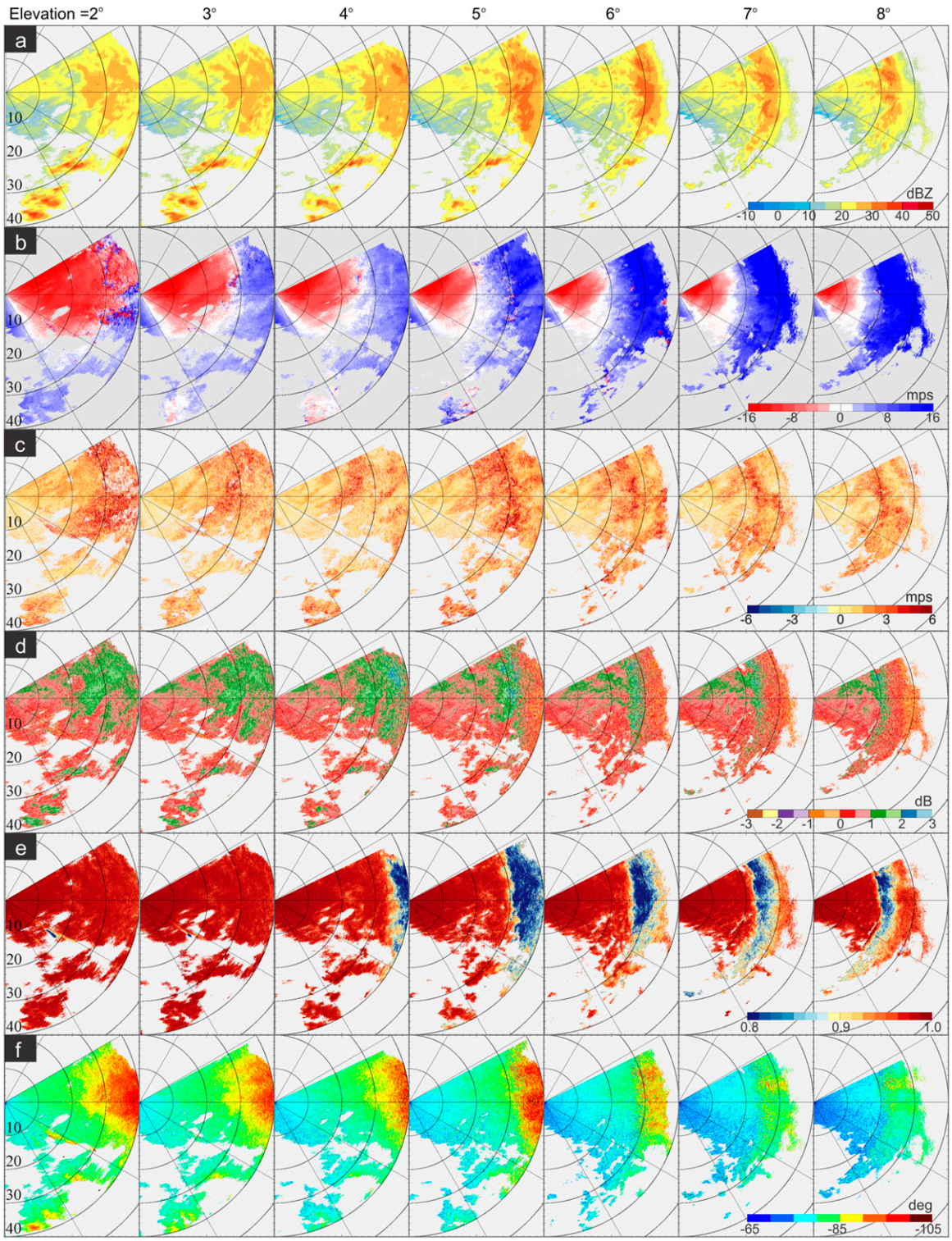

FIG. 5. Stacked sector scans of XPOL-2 while observing stratiform precipitation on 12 Jun 2013 at a range resolution of 30 m within an interval of 2 min. Shown is (a) reflectivity (i.e., Z_h), (b) Doppler velocity v, (c) spectrum width σ_v, (d) differential reflectivity (i.e., Z_{dr}), (e) copolar correlation coefficient (i.e., ρ_{hv}), and (f) differential phase ψ_{dp}.

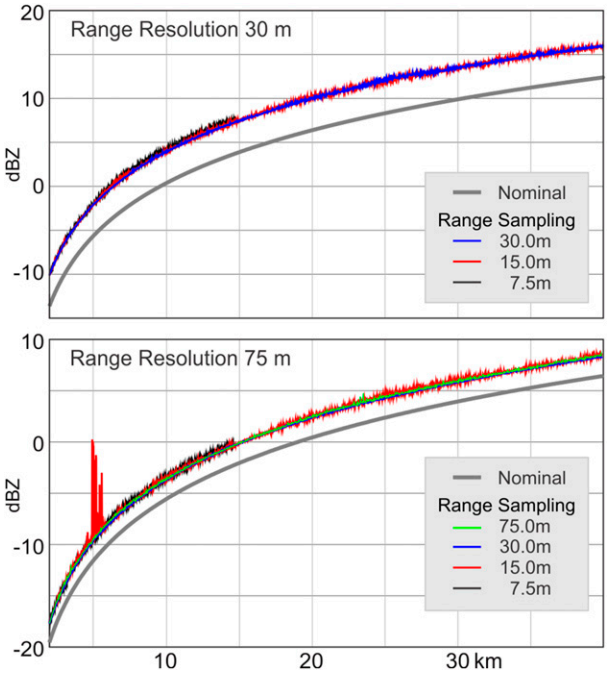

FIG. 6. The min detectable reflectivity (i.e., Z_{min}) of the XPOL-2 radar at different range samplings, as observed at 1939–2331 UTC 12 Jun 2013. The solid gray line indicates the nominal Z_{min} for the range resolution of (top) 30 and (bottom) 75 m. A higher value of Z_{min} indicates lower sensitivity. We have excluded the observed data for the first 2-km range because of the presence of near-range clutter.

interleaving scans at 30 m (and, less frequently, at 15 m). Figure 6 shows the nominal sensitivity of the XPOL-2 radar at 75 and 30 m. To arrive at these curves, we used the parameter values specified in Table 1. Apart from the selectable range resolutions, the XPOL radars have a useful feature for range oversampling as fine as 7.5 m. The range-oversampled samples can be used to accumulate more independent samples without dwelling on the target for a longer duration (see Doviak and Zrnić 1993, 127–128; Torres and Zrnić 2003).

Figure 6 shows the observed sensitivity of XPOL-2 at different range gate spacings or range samplings for the range resolutions 75 and 30 m. For a range sampling of 7.5 m, the number of range gates (for the entire default R_{max} = 40 km) is too large for data to be transferred from the current digital receiver hardware to the signal processor over the Peripheral Component Interconnect Extended (PCI-X) interface. The XPOL radars, therefore, operate at an R_{max} of 15 km when range sampling is set at 7.5 m. The observed XPOL-2 sensitivity in Fig. 6 corresponds to the light-to-moderate rain events at 1939–2331 UTC 12 June 2013. We implemented most of the XPOL-2 scans for this event at Δr = 75 m and a range sampling of 75 m. For Δr = 75 m and range sampling of 15 m, the light rain data were scarcely available in the 4–6 km range, as is apparent from the higher sensitivity values in that range. We note that the difference between the observed and nominal sensitivity values at Δr = 75 m is within 2 dB. On the other hand, this difference is 4 dB for Δr = 30 m, where very few scans were available for the light precipitation profiles.

5. Correction for attenuation

Correction of the measured Z_h and Z_{dr} due to rain attenuation along the propagation path is essential at the X band, especially in convective storms. The method used herein for correcting the measured Z_h is an iterative version of the ZPHI method, which uses a Φ_{dp} constraint (Testud et al. 2000; Bringi et al. 2001) that was originally developed at the C band but later extended to the X band by Park et al. (2005a,b). In short, the coefficient α in the linear relation between the specific attenuation at h polarization A_h and specific differential phase K_{dp} is determined by minimizing a cost function [we refer to Bringi and Chandrasekar (2001), p. 636, for details], whereas the standard ZPHI method uses a fixed a priori value for α (Testud et al. 2000). The optimal estimation of α overcomes its dependence on temperature as well as any potential deviations with respect to the raindrop oblateness from equilibrium theory (Beard and Chuang 1987). There is also some compensation for drop size distributions (DSDs) with above-average values of median volume diameter D_0 (>2.5 mm or so). As in all attenuation-correction schemes based on Φ_{dp}, the correction is approximate since the true DSD along the propagation path is not known. In essence, the optimal α is fixed for a given beam, though improvements are possible if the entire beam is split into smaller-range intervals and the estimation procedure is applied to yield optimal α for each subinterval (Kim et al. 2010). Here, we use the algorithm described in Park et al. (2005b) with modifications for the XPOL-4 radar system. There are many variants of the attenuation-correction method at the X band, as elucidated, for example, by Anagnostou et al. (2004), Matrosov et al. (2005), and Gorgucci and Chandrasekar (2005).

The correction of the measured Z_{dr} for differential attenuation is based on an extension of the method proposed by Smyth and Illingworth (1998) for the C band, which is described in Bringi and Chandrasekar (2001) as a "combined Φ_{dp}–Z_{dr}" constraint. The extension to the X band is described in Park et al. (2005b), which is used herein with some modifications implemented for the XPOL-4 radar. In brief, the A_h determined by the Φ_{dp} constraint is scaled by a factor γ,

and the measured Z_{dr} is corrected for differential attenuation ($A_{dp} = \gamma A_h$) such that a desired value is reached at the end of the beam. The desired value is the intrinsic or ''true'' Z_{dr} at the end of the beam, which is estimated from the corrected Z_h using a mean Z_h–Z_{dr} relation based on scattering simulations that use measured DSDs from several locations that encompass a wide variety of rain types. This sets a constraint for Z_{dr} at the end of the beam (generally $Z_{dr} \sim 0$ dB because of light rain at the end of the beam or because of ice particles above the 0°C level). By the end of the beam, we mean the last range gate where ''meteo'' echoes are detected. Again, the differential attenuation correction is approximate since the true DSD along the beam is not known. Kim et al. (2010) have proposed a method to correct for Z_{dr} by using the iterative ZPHI method to separately estimate A_h and specific attenuation at v polarization A_v (i.e., via the optimal coefficients α_h and α_v; note that $A_{dp} = A_h - A_v$) without using an explicit Z_{dr} constraint at the end of the beam.

The processing steps used here for XPOL-4 data closely follow that detailed by Bringi et al. (2006, 2009) and, hence, we only summarize them.

1) For each range profile (or beam), we generate a data mask to separate precipitation (meteo) from nonprecipitation (non-meteo) echoes by using the standard deviation of Φ_{dp} over a 10-gate moving window. The classification is based on our use of a threshold of 5° and SNR > 0 dB.
2) We corrected the measured Z_h and Z_{dr} values for attenuation, as described earlier.
3) To derive K_{dp}, we first use the iterative range filter methodology applied to each range profile of Φ_{dp}. The finite impulse response (FIR) range filter is, in essence, a weighted moving-average filter in which the weights are determined by the desired magnitude response of the filter transfer function (or spectrum). Here, the FIR filter coefficients are based on 75-m gate spacing [an example of the filter transfer function for 150-m gate spacing can be found in Hubbert and Bringi (1995)]. Note that the XPOL-4 gate spacing is 30 m. The iterative nature of the algorithm described in Hubbert and Bringi (1995) is designed to remove local perturbations in the Φ_{dp} data (e.g., due to the backscatter differential phase) while maintaining the monotonic increase in the propagation phase with the range along the beam. A ''telescoping'' method is used to compute the K_{dp} from the iteratively filtered Φ_{dp} profile, that is, a variable number of gates is used, depending on the Z_h value, to determine the slope of a linear least squares fit (10 gates if $Z_h > 35$ dBZ, 20 gates if $25 < Z_h < 35$, and 30 gates if $Z_h < 25$). Consequently, the ''telescoping'' method is ad hoc but generally corresponds to the ''light'' (9 gates) and ''heavy'' (25 gates) filtering for computing K_{dp} discussed by Ryzhkov et al. (2005).

Since the data processing proceeds one beam (or range profile) at a time, we illustrate in Fig. 7 the range profiles of the measured Z_h and attenuation-corrected Z_h in Fig. 7c, and the same for Z_{dr} in Fig. 7d. The path-integrated attenuation (PIA; from 0 to 20 km) is around 14 dB, while the path-integrated differential attenuation is around 2.7 dB. This example beam is at an azimuth angle of 310° and elevation angle of 10.7° (see Fig. 8). Figure 7a shows Φ_{dp} increasing with range, and $\Delta\Phi_{dp}$ across the rain cell is around 40°. The range-filtered Φ_{dp} from which K_{dp} is calculated is also shown. The coefficient α for this beam is then 14/40 = 0.35 dB $(°)^{-1}$, whereas the coefficient β (in $A_{dp} = \beta K_{dp}$) is 2.7/40 = 0.067 dB $(°)^{-1}$. Figure 7b shows the K_{dp} profile, with peak K_{dp} around 5.6° km^{-1} at a range of 12 km; the corresponding corrected Z_h and Z_{dr} are 52.8 dBZ and 2.2 dB, respectively. Figure 7b also shows the data mask for this particular beam (1 for meteo and 0 for non-meteo echoes). The rain rate from K_{dp} can be derived from $R = 14.2K_{dp}^{0.85}$, which yields 60 mm h^{-1}, whereas $Z_h = 320R^{1.55}$ with $Z_h = 52.8$ dBZ also yields close to 60 mm h^{-1}. The coefficients/exponents of the $R(K_{dp})$ and $R(Z_h)$ power laws are derived from 2DVD-measured DSDs from 4 days during IFloodS and scattering simulations using the T-matrix method, assuming the drop shapes from Thurai et al. (2007) and a Gaussian distribution of canting angles with (with mean canting angle = 0° and standard deviation = 7.5°) from Huang et al. (2008). The agreement between $R(K_{dp})$ and $R(Z_h)$ in this particular range gate is perhaps fortuitous, but it also indicates that the Z_h attenuation correction is reasonable (if the measured Z_h of 42 dBZ had been used, the corresponding R would have been seriously underestimated at 12 mm h^{-1}), thereby indicating the well-known importance of attenuation correction at the X-band even if Z–R relations are subsequently used to quantify rainfall amounts.

Figure 8 shows the PPI scan of corrected Z_h at an elevation angle of 3°, which depicts the large spatial variability in this highly convective rain cell complex at 2334 UTC. The peak Z_h is in the range 55–60 dBZ. Figure 9 shows the rain accumulation field integrated from 2241 to 0034 UTC using the $R(K_{dp})$ power law given earlier. In spite of the smoothing that is inherent in deriving the K_{dp} field, the rain accumulation ''map'' shows reasonable spatial variability with maximum accumulation of 28 mm with few artifacts due to non-meteo

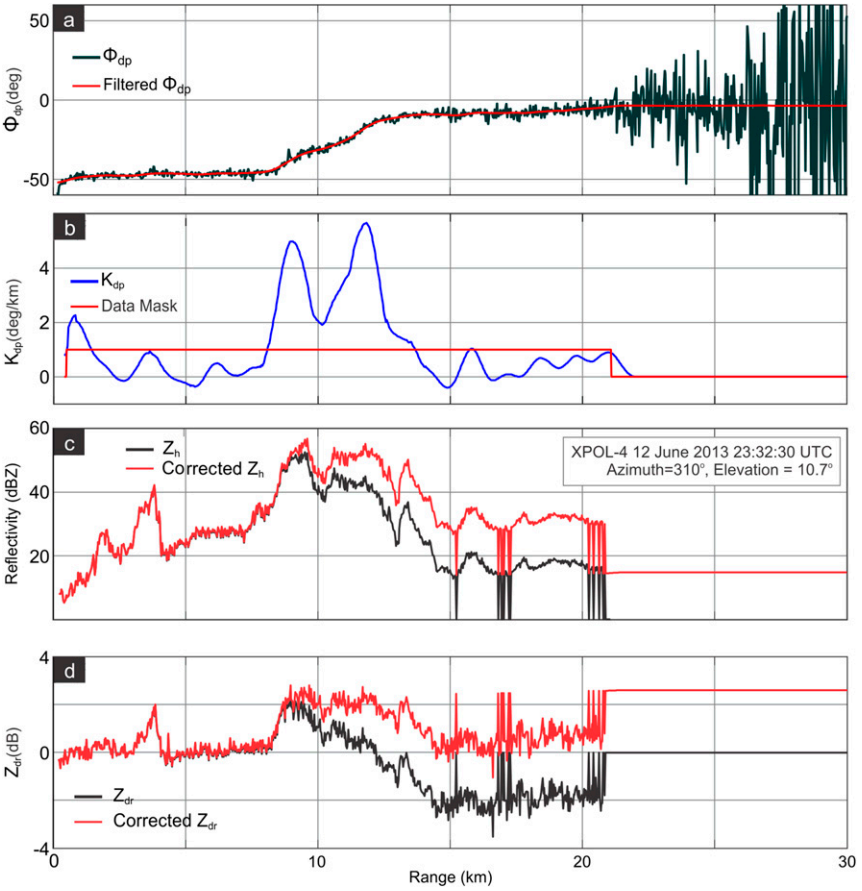

FIG. 7. Example range profile from the XPOL-4 radar during IFloodS at 2332 UTC 12 Jun 2013, azimuth = 310°, and elevation = 10.7°. In (a), "filtered" denotes FIR range filtered Φ_{dp}. In (b), the data mask value of 1 ≡ meteo echoes and 0 ≡ non-meteo echoes (in this beam, the latter is receiver noise). In (c) and (d), "corrected" denotes attenuation-corrected values. See also the PPI scan in Fig. 8 to locate the radial at 310°.

echoes. The beam blockages surrounding a small azimuth sector centered at 300° and 330° are evident in Fig. 8.

Figure 10 depicts RHI scans at an azimuth angle of 310° (along the radial to the XPOL-2 radar) and illustrates the measured Z_h (Fig. 10, top) and corrected Z_h (Fig. 10, bottom) values. Similarly, Fig. 11 shows the measured Z_{dr} and corrected Z_{dr} values, while the K_{dp} field is in Fig. 12. The following points can be made by examination of these plots. The necessity for attenuation correction of Z_h (from an RHI perspective) is obvious when comparing Fig. 10 (top and bottom), especially below a 4-km height (the 0°C height is around 4.7 km based on the nearby sounding carried out at 0000 UTC 13 June 2013 by the National Weather Service station in Davenport, Iowa, about 217 km away from and 100 m in elevation lower than the St. Olaf location of XPOL-4). Moreover, the signal becomes extinct starting at a range of 14 km and a height of 4 km, and no further correction is possible. The strong convective nature of the storm complex is evident in the tall column of high Z_h values reaching at least 8 km in height. Correction of the measured Z_{dr} for differential attenuation is well illustrated in the vertical direction by comparing Fig. 11 (top and bottom). It is difficult to fully correct for both attenuation and differential attenuation near the melting layer (3.5–4-km height interval), as this is a mixed-phase region, that is, rain mixed with melting graupel (Tabary et al. 2009). The path-integrated attenuation will be the sum attributable to both rain and wet ice, whereas the Φ_{dp} is due to the rain component alone (wet ice being nearly spherical). Thus, a Φ_{dp} constraint is not sufficient and dual-wavelength techniques become necessary (S/X-band radar) to separately estimate the PIA due to rain and wet ice near the melting layer. The vertical structure of K_{dp} in Fig. 12 is interesting since the maximum values (6°–8° km^{-1}) are

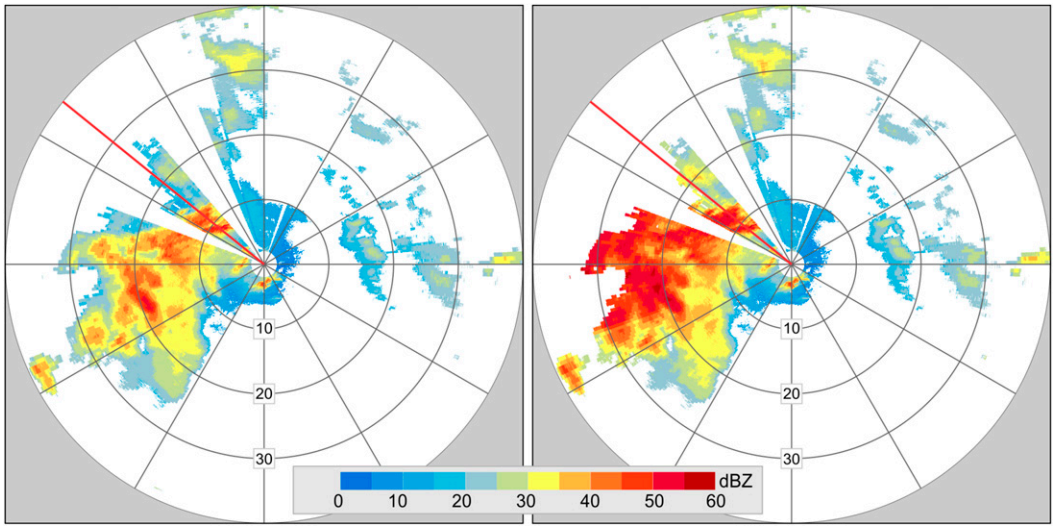

FIG. 8. The PPI scan of the (left) measured and (right) attenuation-corrected Z_h field at 2334 UTC 12 Jun 2013. The origin is the location of the XPOL-4 radar. Positive (negative) distances along the horizontal axis correspond to the east (west) of the radar. Similarly, positive (negative) distances along the vertical axis correspond to the north (south) of the radar. The solid red line indicates the vertical RHI profile at azimuth = 310° (IFloodS data portal file identifier: MXPOL4-polar-20130612–233401-PPI-003_0.nc).

located aloft near 2.8 km, which implies that the maximum rainwater content has not yet descended to the surface. The examples shown here illustrate the high quality of polarimetric radar data from the X-band radar (XPOL-4).

6. Simultaneous multiple-view observations by XPOL radars

The key objective of the pairwise deployment of the Iowa XPOL radars during IFloodS was to mitigate the effect of attenuation at the X band. If the data from one XPOL unit suffers from attenuation at far range, the same can be recovered by the second XPOL unit in the latter's near range. This approach is considered desirable when both XPOL radars are identical and properly calibrated units. We observed a number of vertical profiles in the common precipitation volumes of XPOL-2 and XPOL-4 during IFloodS. Here, we present comparisons for two different storms in order to illustrate both the advantage of using 30-m resolution in the X-band and the excellent calibration of the Iowa XPOL units. As shown in Fig. 1, XPOL-2 and XPOL-4 share an overlapping coverage over a range of 34 km (i.e., only 6 km of range coverage of one unit is excluded from the coverage of the other unit). In the following, we compare the RHI plots for the two radars. When the two radars are pointing toward each other, the azimuthal angles are 120° and 310° with respect to XPOL-2 and XPOL-4, respectively.

a. Different range resolutions, identical pulsing schemes: Stratiform rain observations

Figure 13 shows a series of plots that compare the vertical profiles of the same stratiform rain event observed by XPOL-2 and XPOL-4 data on 26 May 2013. The XPOL-2 RHI scan corresponds to 1451 UTC and

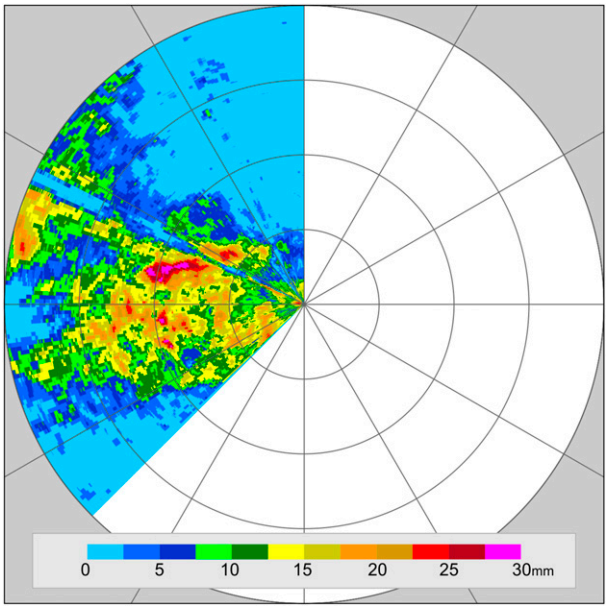

FIG. 9. The rain accumulation field (mm) from 2241 to 0034 UTC 12 Jun 2013 derived from K_{dp} using $R = 14.2K_{dp}^{0.85}$. Range rings are spaced 10 km apart.

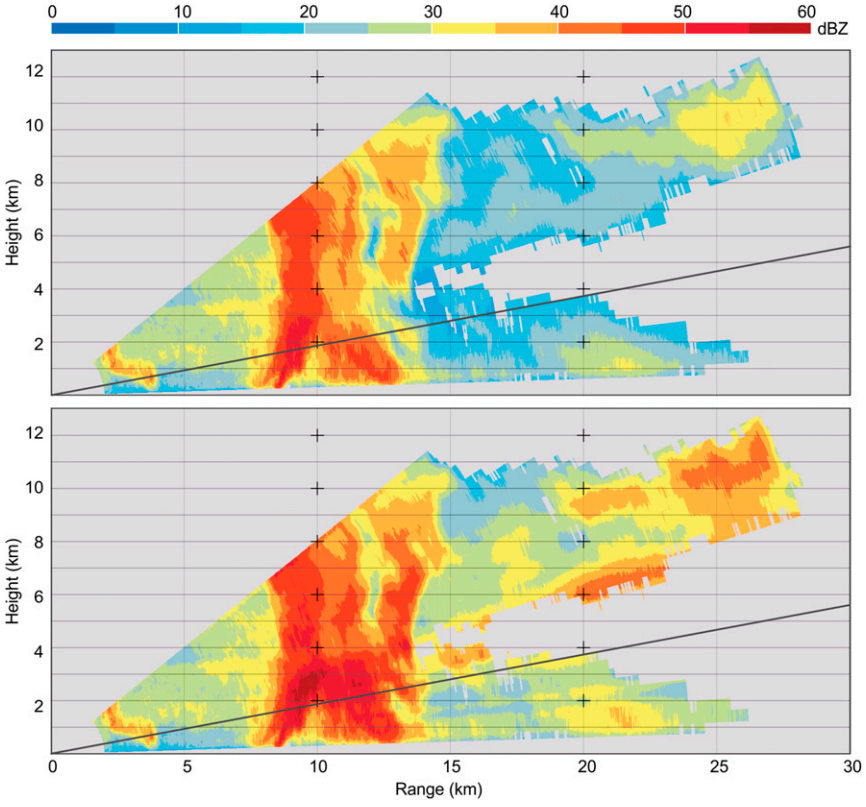

FIG. 10. The RHI scan of (top) measured and (bottom) attenuation-corrected Z_h along the azimuth = 310° (radial toward the XPOL-2 radar site). The solid gray line indicates the ray profile at an elevation of 10.7° (IFloodS data portal file identifier: MXPOL4-polar-20130612–233230-RHI-309_9.nc).

that of XPOL-4 to 1452 UTC. The XPOL-2 data were collected at a range resolution of 75 m, while the same was collected at 30 m for XPOL-4. We note that the XPOL-4 data show detailed features of the storm in the Z_h plot (Fig. 13b). Figure 13 also shows a reasonable match of the Doppler velocity profiles for the two radars. Both radars operated at a staggered PRT (950/1200 μs) mode that yields a maximum unambiguous Doppler velocity of $\approx$32 m s^{-1}. In Fig. 13d, the direction of the Doppler velocity for XPOL-4 has been reversed to enable convenient comparison with the XPOL-2. In Figs. 13e and 13f, the differential reflectivity for both the radars has been corrected using the calibration factor obtained from the nearest (in time) vertical-pointing scan for the light rain. Both radars depict the existence of a continuous brightband structure over a total 46-km range, as evidenced by similarities in the Z_{dr} and copolar correlation coefficient plots. The weaker signal areas of XPOL-2 in its far range are observed without any degradation in signal quality by the XPOL-4. However, none of these plots employs the method of correction for attenuation that is described in the previous section. We also inspected the data for this event from the closest WSR-88D at La Cross, Wisconsin. The beam height of the WSR-88D exceeds ~2 km over Turkey River (~100-km range) and Cedar River (>150-km range) basins, and it is difficult to observe the brightband structure over these regions with WSR-88D data.

b. *Same range resolutions, different pulsing schemes: Convective rain observations*

We now compare the XPOL-2 and XPOL-4 observations in the common precipitation volume when the two radars operated at the same range resolution of 30 m. This comparison also allows us to compare the profiles after they have been corrected for the attenuation using the method described in section 5. Figure 14 shows the comparison of vertical profiles for a convective rainstorm by XPOL-2 and XPOL-4 on 12 June 2013. The XPOL-2 observations correspond to 2318 UTC, differing by only a minute from XPOL-4 observations at 2319 UTC. The reflectivity plots for both radars show remarkable similarities, with XPOL-4 also recovering the echoes in the 20–30-km range. The convective storm complex was in the near-range of XPOL-2 that consequently suffered more attenuation in the common

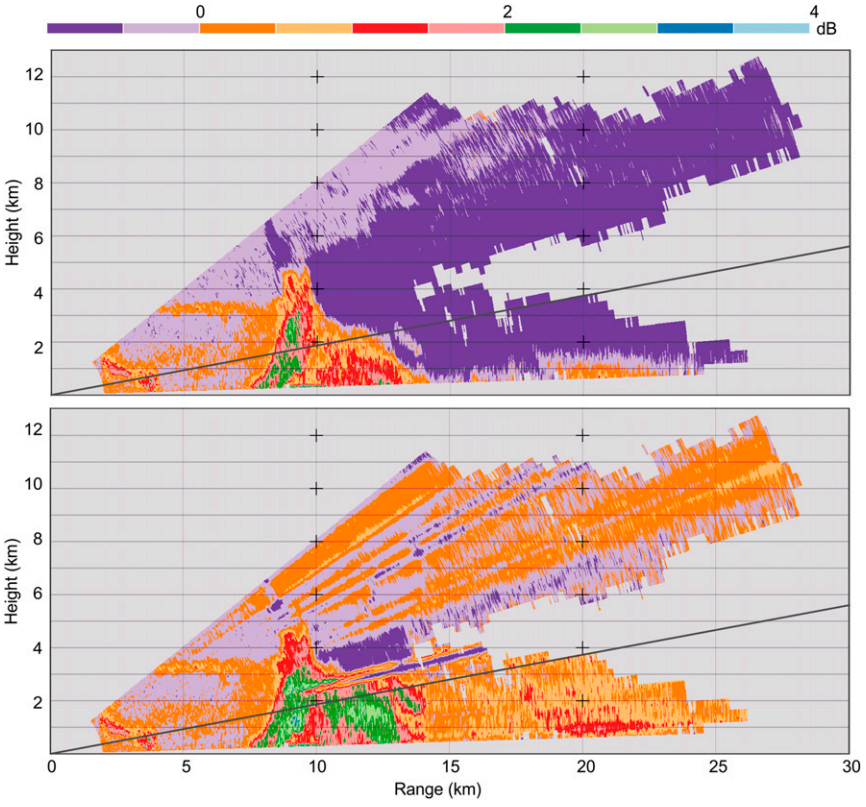

FIG. 11. As in Fig. 10, but for Z_{dr}.

volume. Other polarimetric estimates in Fig. 14 show similar dispersions and similar vertical structures in the 10–20 km range for both radars. The left and middle columns show a comparison of distributions of corrected polarimetric estimates (Z_h, Z_{dr}) and K_{dp} for XPOL-2 and XPOL-4. For this comparison, we have selected the region within the range of 6–20 km and height 1–5 km (marked by the gray box in the corrected Z_h graphs of Fig. 14), so that the $\rho_{hv} \geq 0.9$ and XPOL-2 signal was not completely extinct. We obtained the following standard deviations within this region:

1) corrected Z_h, 6.4571 (XPOL-2) and 4.8292 (XPOL-4);

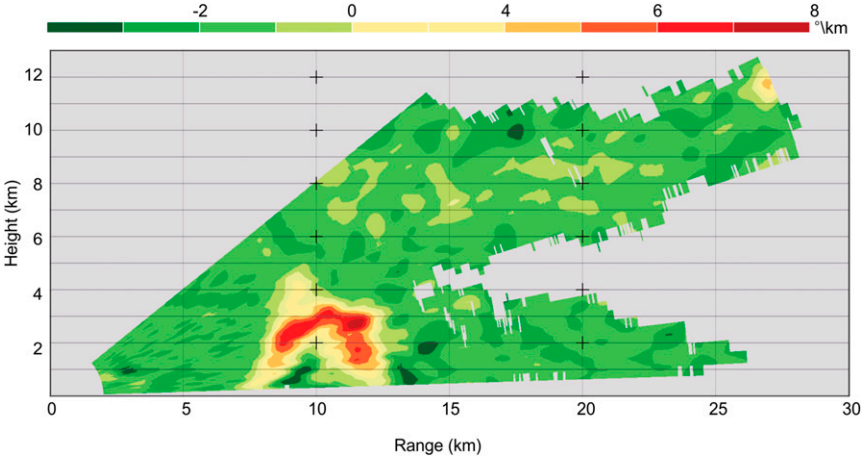

FIG. 12. Specific differential phase K_{dp} for the same scan as in Fig. 10.

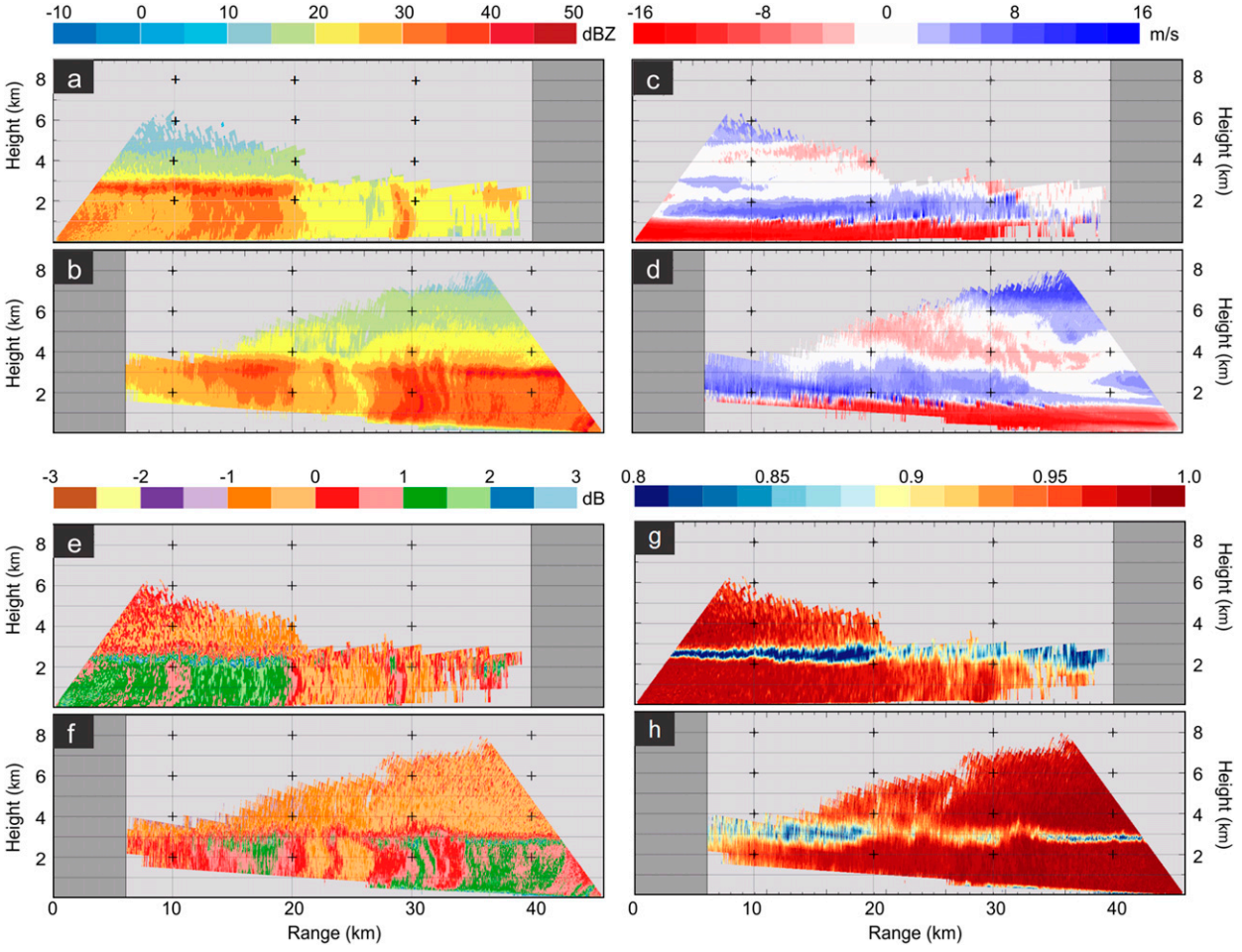

FIG. 13. Near-simultaneous observations of common precipitation volume by (a),(c),(e),(g) XPOL-2 and (b),(d),(f),(h) XPOL-4 on 26 May 2013. Shown are (a),(b) Z_h; (c),(d) Doppler velocity; (e),(f) Z_{dr}; and (g),(h) ρ_{hv} data. The XPOL-2 and XPOL-4 were operating at range resolutions of 75 and 30 m, respectively.

2) corrected Z_{dr}, 0.5273 (XPOL-2) and 0.6471 (XPOL-4); and
3) K_{dp}, 0.6239 (XPOL-2) and 0.6306 (XPOL-4).

The XPOL-2 radar operated at a uniform PRT of 1000 μs, while the XPOL-4 used staggered PRT (950/1200 μs) during this scan. Therefore, this comparison does not include the Doppler velocity, which would obviously not match across the two radars for this configuration.

7. Comparisons with 2DVD-based data

The IFloodS campaign included six 2DVD units all installed along the southeast radial (at approximately 131° azimuth) of the NPOL radar in the range of 5–106 km. Three of these units were within the XPOL-5 coverage, the closest unit being 2DVD-SN38 (~12 km away from the XPOL-5 radar). To assess the data quality of XPOL-5 and the accuracy of the attenuation-correction procedures, we have used data from the aforementioned 2DVDs for comparison against the XPOL-5 measurements over the corresponding locations.

Here, we consider the stratiform rain event of 26 May 2013 that lasted for many hours over the XPOL-5 coverage area. The XPOL-5 made full PPI sweeps during the entire event timeline. Figure 15a shows the reflectivity data extracted from each PPI scan over the SN38 location, including four neighboring pixels (i.e., two adjacent beams and two adjacent range gates), as a time series. Figure 15b shows the corresponding differential reflectivity data. We remark that the Z_h and Z_{dr} data in Figs. 15a and 15b are obtained after applying the attenuation-correction procedures described earlier in section 5. Figure 15c shows the values of K_{dp} derived from the differential propagation phase measurements. In all three cases, we use a simple averaging procedure in order to reduce the spatial and temporal fluctuations.

Superimposed on these plots are the curves obtained from the scattering calculations based on the 2DVD

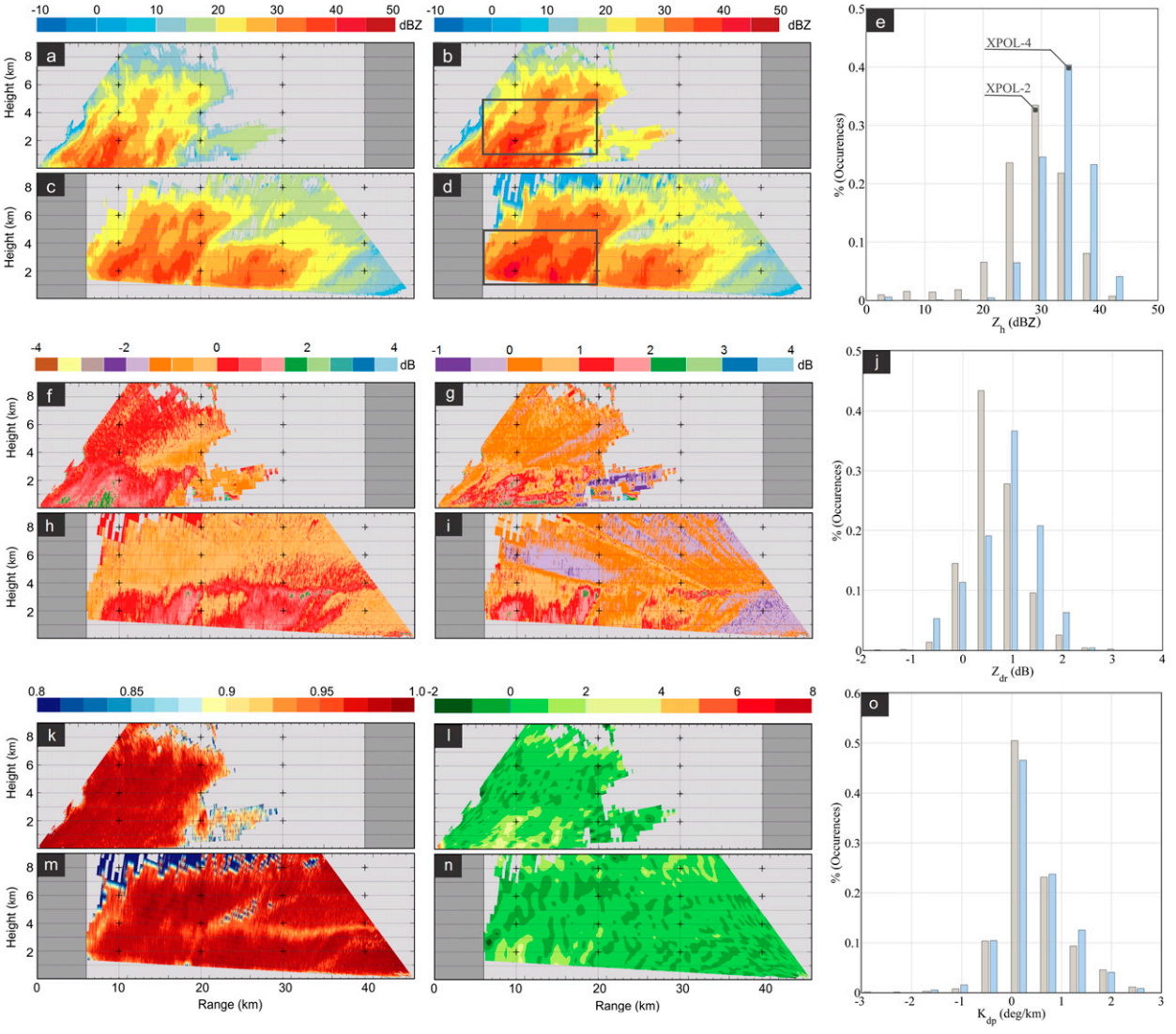

FIG. 14. Near-simultaneous observations of common precipitation volume by (a),(b),(f),(g),(k),(l) XPOL-2 and (c),(d),(h),(i),(m),(n) XPOL-4 on 12 Jun 2013 at the same range resolution. The plots show (a),(c) uncorrected Z_h; (b),(d) corrected Z_h; (f),(h) uncorrected Z_{dr}; (g),(i) corrected Z_{dr}; (k),(m) ρ_{hv}; and (l),(n) K_{dp}. For the region marked by the gray box in corrected Z_h RHIs, the histograms compare XPOL-2 and XPOL-4 data for (e) corrected Z_h, (j) corrected Z_{dr}, and (o) K_{dp}.

data. For the scattering (T-matrix) calculations based on 1-min DSDs, we assumed our reference drop shapes (Thurai et al. 2007) that are representative of the most probable shapes for drop equi-volume diameters up to 7 mm, as well as a 6° standard deviation for the Gaussian distribution of drop canting angles (Huang et al. 2008). We also note that we have smoothed the 2DVD-based calculations over 3 min using a uniformly weighted moving average (three 1-min samples).

We used the same 1-min DSDs as input to the T-matrix simulations for XPOL-5 to derive rain-rate estimators based on the radar parameters. We considered the following algorithms for evaluation here:

1) estimator 1 is $Z_h^{\text{linear}} = 350.3R^{1.56}$,
2) estimator 2 is $R(K_{dp}) = 15.5K_{dp}^{0.89}$, and
3) estimator 3 is $R(A_h) = 47.6A_h^{1.0565}$.

The A_h is the X-band specific attenuation for h polarization and is derived from the ZPHI method. Its advantages are similar to those of K_{dp} except that it is unsmoothed in range and not immune to the presence of hail. [Please see Bringi and Chandrasekar (2001, p. 636) for details on the relationship between A_h and K_{dp}.] We follow the recommendations of Ryzhkov et al. (2014) for computing $R(A_h)$, which is relatively less sensitive to DSD variability. However, our formulas are tuned to the

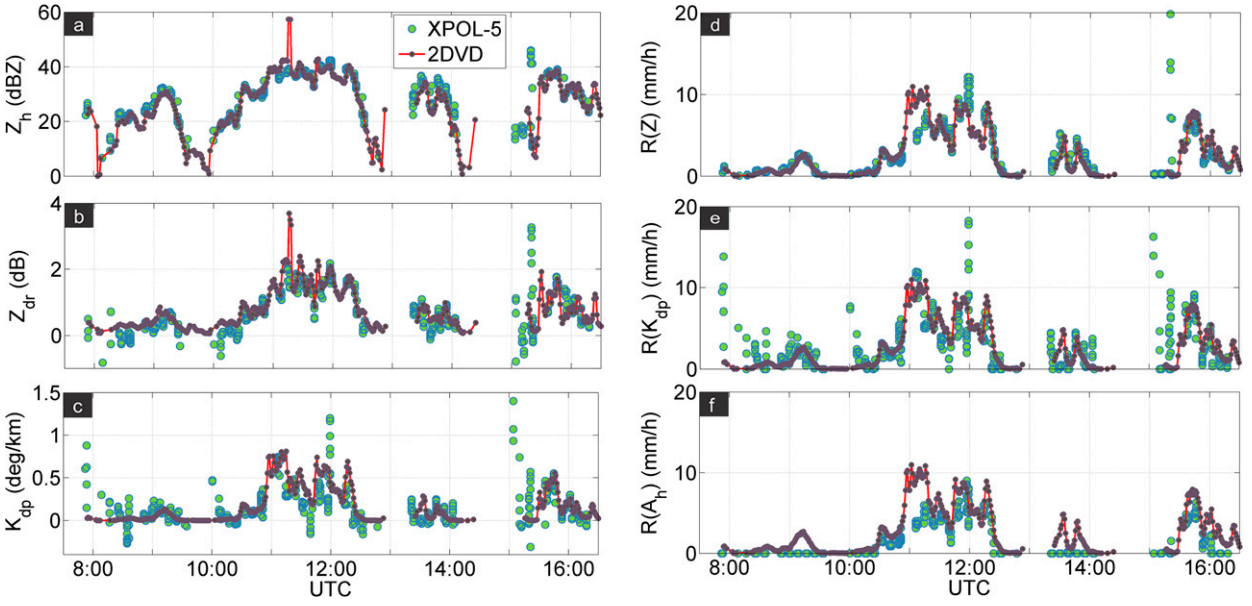

FIG. 15. Comparison of XPOL-5 and 2DVD-based data. Shown are (a) Z_h, (b) Z_{dr}, (c) K_{dp}, and rain-rate estimates using estimator (d) 1, (e) 2, and (f) 3.

IFloodS events since we use the 2DVD data for our scattering simulations.

We applied these estimators to the XPOL-5 data (after attenuation corrections) and compared them with the estimators derived directly from the 2DVD measurements. Figures 15d–f show a close agreement for all three estimators, clearly demonstrating the data quality of the XPOL radar. We intend to quantify the accuracy of each of these estimators (and a few other estimators not shown here) and their composite algorithm in more detail in the future. We also note that the Z_h and Z_{dr} comparisons in Fig. 15 can be used to derive the radar calibration offsets, as has been done previously for NPOL during the Midlatitude Continental Convective Clouds Experiment (MC3E) campaign (Bringi et al. 2013). Later, Thurai et al. (2013) also showed that this technique when applied to NPOL data during one IFloodS event gave consistent results with the well-established self-consistency method.

Finally, Fig. 16 shows PPI sweeps from XPOL-5 and NPOL for nearly concurrent scans that are only a minute apart. For the NPOL sweep, we show the data only over the XPOL-5 coverage area. The two radars show reasonably good resemblance although they are not identical. This is expected since the two radars have different frequency bands and are located more than 75 km apart. Further, both radars also have different sample volumes (by virtue of the different elevation angles and the distances involved) of different dimensions because of different beamwidths and range resolutions. The XPOL does, of course, show finer and more detailed rainfall structure because of its high-range sampling. This will be potentially useful for examining the finescale structure of precipitation in terms of the spatial correlations of both rainfall rate and the DSD parameters. For example, Bringi et al. (2015) have already successfully derived relatively coarser-scale spatial correlation structures for two events during the MC3E campaign using repeated NPOL PPI and RHI scans over a network of 2DVDs.

8. Summary

The deployment of the Iowa XPOL radars during IFloodS achieved a number of goals. The IFloodS campaign generated vast and unprecedented radar data (see Fig. 2) at high spatiotemporal resolutions, as presented in this paper. The data collected by the XPOL radars are available online to the GPM community members through the Iowa Flood Information System (IFIS) and NASA's IFloodS web portal (Demir et al. 2015).

The engineering tests (see appendix) established the stability of the XPOL transmitter output within 2 dBm over long hours of operation, a wide receiver dynamic range (~70 dB), and good calibration using external targets and sources. These tests followed GPM GV protocol, thereby proving suitability of XPOL radars for future campaign participation. The raw data analysis showed 99% fit of I/Q samples to the model distributions

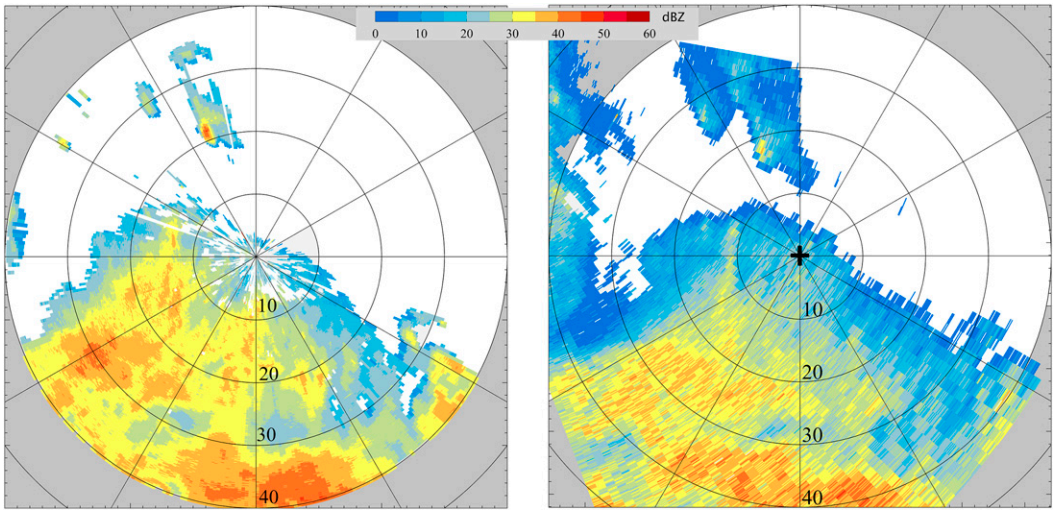

FIG. 16. Comparison of (left) XPOL-5 and (right) NPOL reflectivities observed during scans at 0908 and 0909 UTC 26 May 2013, respectively. For NPOL, only the data over the XPOL-5 coverage area are shown (the black plus sign marks the location of the XPOL-5).

and absence of I/Q imbalance. The stratiform rain observations (presented in section 4b), where the entire sector volume scan was completed in less than 3 min at 30-m range resolution, established XPOL's capability to make precipitation observations at high spatiotemporal resolution. The sensitivity analyses at 7.5-m range sampling show degradation within 1–2 dBZ. The inter-XPOL comparison of attenuation-corrected and derived products in the common volume reveals between-radar differences in standard deviations of ~1.5 dBZ for Z_h, 0.12 dB for Z_{dr}, and 0.01° km^{-1} for K_{dp}. This demonstrates excellent common-volume match between XPOL-2 and XPOL-4, further attests to the good calibration of XPOL radars, and shows effectiveness of our attenuation-correction algorithm. The rainfall rates based on XPOL-5 data showed close agreements with 2DVDs for all three different algorithms derived from T-matrix simulations. The high-resolution XPOL data exhibited detailed precipitation structures that were not observed by S-band radars (NPOL and WSR-88D) over the Turkey River and Clear Creek basins. Through analysis of the data collected during IFloodS, we demonstrated physical consistency of the polarimetric observables collected by the XPOL radars. The observable quantities agree very well with the same quantities calculated from DSD data collected using disdrometers (D'Adderio et al. 2015; Gatlin et al. 2015).

The XPOL-2 and XPOL-4 pair operated for more than 90% of the campaign duration without any major engineering issues and was operational (remotely controlled and remotely monitored) during almost all precipitation events. This uninterrupted operation of the XPOL-2 and XPOL-4 units during the campaign demonstrates the robust engineering design and field worthiness of these radars. In particular, we have achieved an overarching objective to mitigate attenuation through the pairwise deployment of radars. Note that while an application of the well-established attenuation-correction techniques for X-band polarimetric radars is limited by the sensitivity of these units, a pairwise deployment allows reconstruction of a rain storm over a wider area. In this paper, we merely illustrated this on a couple of cases, and a more comprehensive analysis of the entire dataset is in progress. Also, it will be interesting to recover the same data using all four units in future campaigns, especially when the signal from one of the radars becomes extinct.

FIG. 17. This rotary joint is more robust than the original flexible waveguides. All XPOL units have been upgraded after the IFloodS campaign to operate with the rotary joints.

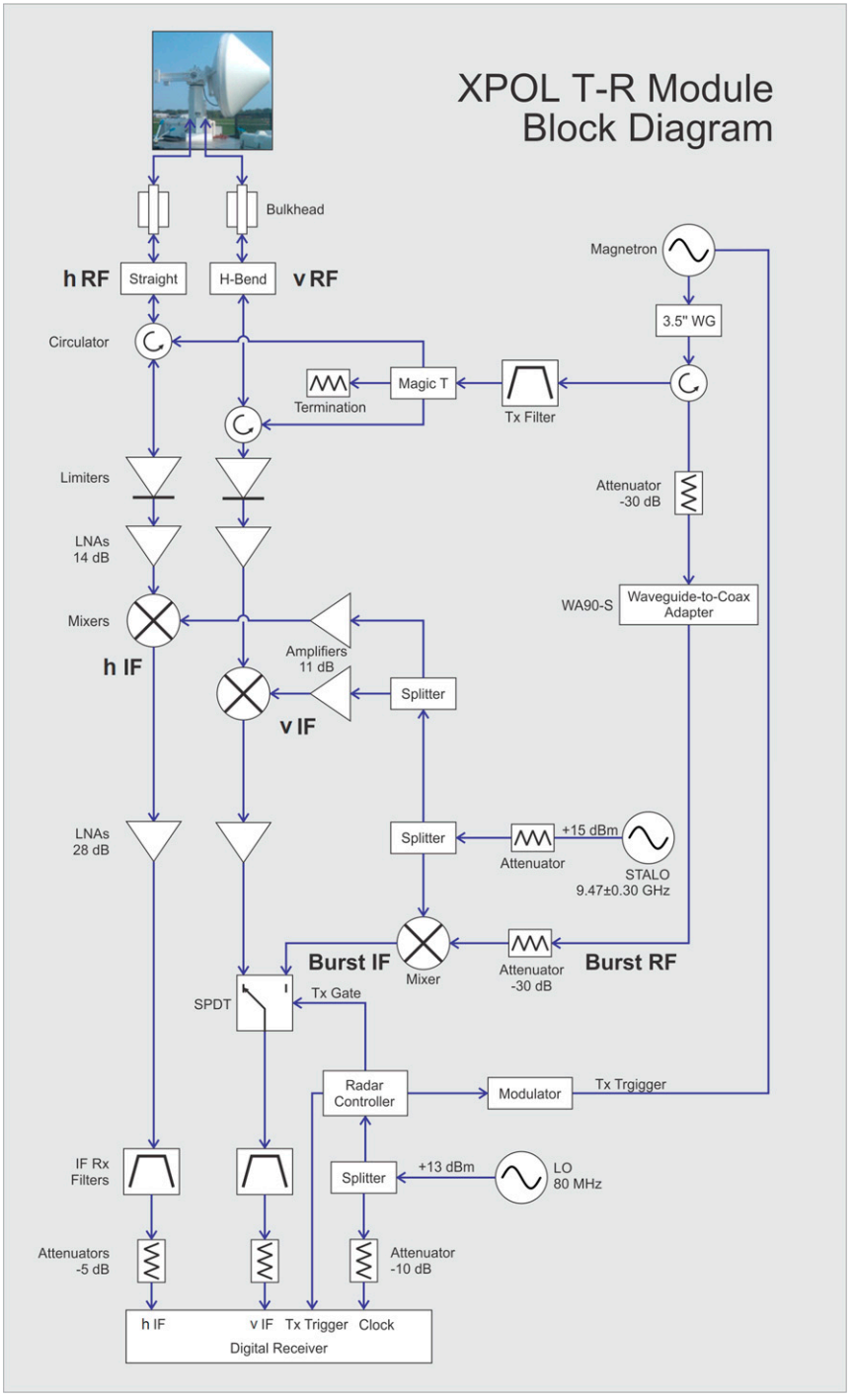

FIG. A1. Schematic diagram of a typical XPOL unit. The RF and digital hardware resides in an environmentally controlled enclosure that is mounted on the radar trailer.

Last but not least, we demonstrated that the radars are capable of providing useful data at very high spatial resolution, as high as 7.5 m along a radial. While rainfall estimation for hydrologic application may not benefit from this high resolution, hydrometeorological studies and fundamental studies on rainfall properties clearly could.

We are further analyzing the calibration of the Iowa XPOL radars by comparing the polarimetric estimates with the NASA S-band polarimetric (NPOL) radar. The

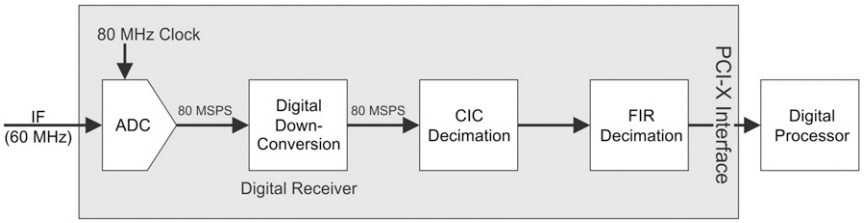

FIG. A2. The 80-MHz analog-to-digital converter (ADC) of the digital receiver subsamples the bandpass-filtered IF signal at 60 MHz. The digital receiver chain is shown here for only one polarization.

NPOL radar was collocated in the IFloodS region with the Iowa XPOL radars (see Fig. 1), and the Iowa XPOL-2 and XPOL-4 units were deployed in the far range of the NPOL. Our objective is to use Iowa XPOL products and collocated rain gauges to provide rainfall estimates at those far ranges of NPOL. This approach yields anchor points for NPOL rainfall estimates with respect to fulfilling key goals of NASA's GPM Ground Validation program.

Following the IFloodS campaign, we decided to replace the flexible waveguides with rotary joints that were procured from Pasquali Microwave Systems and custom fit to XPOL pedestals (Fig. 17). Consequently, we upgraded the XPOL system software with additional capabilities for the spectral processing [fast Fourier transform (FFT)] modes that we intend to deploy during the data collection operations in the future. To determine the new radar constant, we conducted the aforementioned engineering tests on the XPOL units again during August 2014. The digital receiver units for all XPOL units are currently being upgraded to provide digital noise floor on the order of −84 dBm (compared to −70 dBm during IFloodS).

The XPOL radars will participate in a future hydrology-oriented campaign currently under discussion with members of the research community. The XPOL-3 and XPOL-5 units are undergoing refurbishment and testing in order to operate without any data

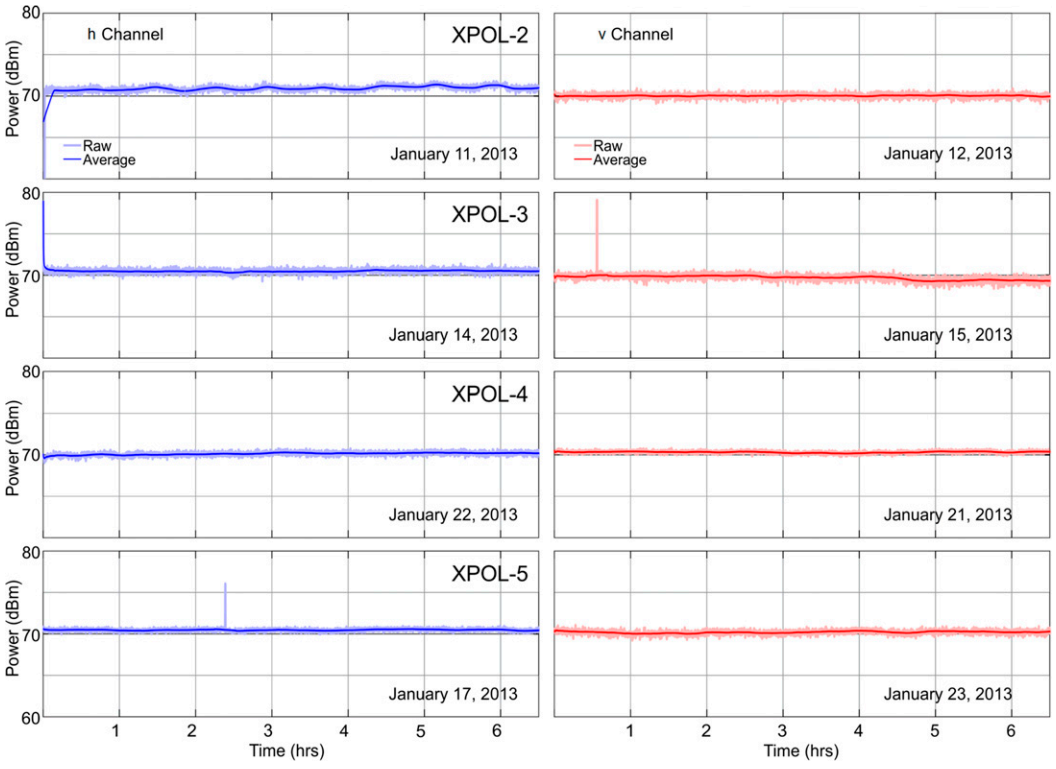

FIG. A3. The transmit power log of Iowa XPOL radars as recorded during January 2013. The occasional spiky data are due to a time reset on the power meter reading at the midnight hour. The "average" indicates a 1-min average of the 5-s "raw" measurements.

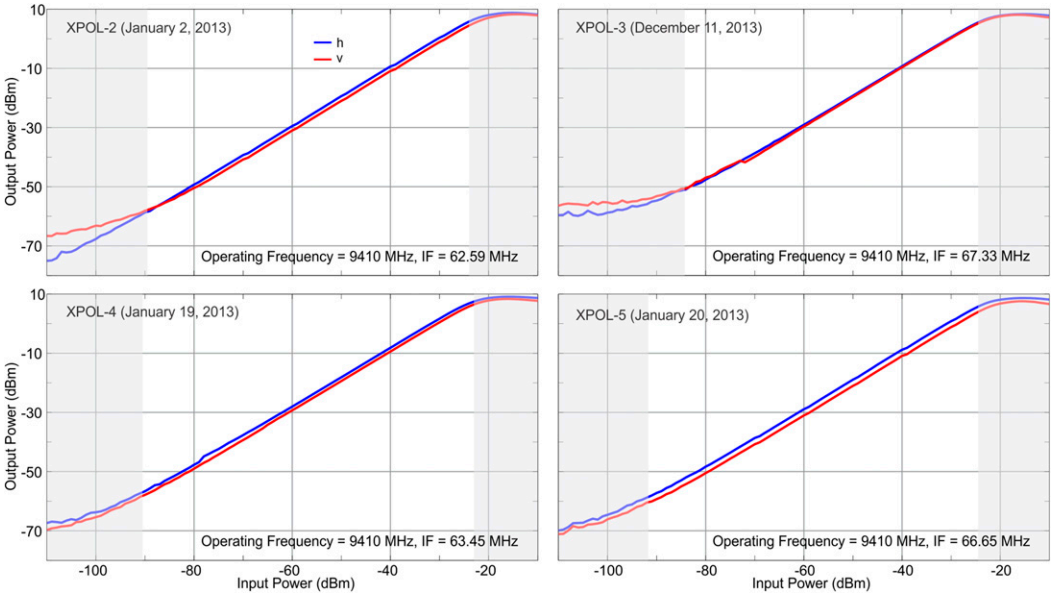

FIG. A4. Power sweeps of the entire receiver chain show the linear operation of the receiver over a wide average receiver dynamic range.

artifacts. The XPOL-2 unit continues its deployment at one of the home XPOL radar locations in Iowa City.

Acknowledgments. This study was supported by the Iowa Flood Center, the National Science Foundation (RAPID) Award 1327830, and NASA's Global Precipitation Measurement program through Awards NNX13AG94G and NNX13AD83G. V.N.B. and L.T. acknowledge support via NNX13AI94G and NNX14AJ81G.

APPENDIX

Technical Characterization of Iowa XPOL Radars

a. Details of XPOL hardware

Figure A1 shows a detailed block diagram of the transmit–receive subsystem of the units. A modulator controls the firing of the magnetron transmitter, whose output frequency is nominally centered around 9.41 GHz. The receiver is composed of two physically separate, identical radio frequency (RF) hardware paths consisting of an assembly of microwave limiters and low noise amplifiers (LNA). The output of the radar stable local oscillator (STALO)—in this case, a dielectric resonant oscillator (DRO)—is passed through a receiver splitter to the microwave mixers of horizontal and vertical polarization chains in order to translate the signal from the RF to an intermediate frequency (IF) of 60 MHz. The transmit signal is also translated to 60 MHz and then sampled in the v-channel IF using a single-pole-double-throw (SPDT) switch that is located before the microwave IF filters. A digital receiver subsamples the 60 MHz IF signal at the sampling rate of 80 mega samples per second (MSPS; Fig. A2). For an overview of the theory and detailed operation of weather radar digital receivers and related terminology used here, please refer to Mishra (2012). The down-converted in-phase and quadrature-phase data are downsampled using a cascaded integrator–comb (CIC) filter chain and are eventually filtered by a finite-impulse response (FIR) decimator operating at a programmable bandwidth and decimation rate. For 75-m range resolution, the bandwidth is set at 2 MHz. The digital data processor receives the I/Q time series data over a PCI-X interface.

b. Engineering evaluation

During the period from December 2012 to January 2013, prior to the field deployment of the Iowa XPOL radars, we conducted extensive engineering calibration and tests of all the units to prepare the radars for campaign-level operations in broad conformity with the guidelines of NASA GPM Ground Validation (Hou et al. 2008; Chandrasekhar et al. 2014). The tests included measurement of the transmit power and spectrum, receiver frequency response, cross-channel isolation, characterization of drifts in DRO over time,

measurement of digital noise floor, and sphere calibration and solar scans (Mishra et al. 2013). Because it is not possible to summarize the findings and test results for all four radars here, we chose a few of them to demonstrate the technical robustness of the radar system.

The stability of the magnetron output over longer durations is a critical parameter with respect to ensuring the desired operation of the XPOL radars. We used a calibrated assembly of 45-dB directional coupler, 30-dB coaxial attenuator, Agilent 8481A power sensors, and Agilent E4419B power meter in duty cycle mode to record the transmit power. We observed a good degree of stability in the transmit output, as shown in the log of the transmit power for several hours (the measured power has been recalibrated to its supposed value at the waveguide port by deducting the losses incurred by the coupler–attenuator–sensor assembly from the measurements of the power meter; Fig. A3). We also measured the response of the analog receiver by injecting a continuous wave (CW) signal into the waveguide port of the RF box using an Agilent 83640B signal generator and then recorded the IF output with an Agilent E4440A spectrum analyzer. Figure A4 shows the linear operation of the analog receiver over a wide dynamic range. The digital receiver noise floor for the radars at the time of this experiment was slightly below −70 dBm.

REFERENCES

Anagnostou, E. N., M. N. Anagnostou, A. Kruger, W. F. Krajewski, and B. Miriovsky, 2004: High-resolution rainfall estimation from X-band polarimetric radar measurements. *J. Hydrometeor.*, **5**, 110–128, doi:10.1175/1525-7541(2004)005<0110:HREFXP>2.0.CO;2.

Battan, L. J., 1973: *Radar Observation of the Atmosphere*. University of Chicago Press, 324 pp.

Beard, K. V., and C. Chuang, 1987: A new model for the equilibrium shape of raindrops. *J. Atmos. Sci.*, **44**, 1509–1524, doi:10.1175/1520-0469(1987)044<1509:ANMFTE>2.0.CO;2.

Berne, A., and R. Uijlenhoet, 2006: Quantitative analysis of X-band weather radar attenuation correction accuracy. *Nat. Hazards Earth Syst. Sci.*, **6**, 419–425, doi:10.5194/nhess-6-419-2006.

Borque, P., P. Kollias, and S. Giangrande, 2014: First observations of tracking clouds using scanning ARM cloud radars. *J. Appl. Meteor. Climatol.*, **53**, 2732–2746, doi:10.1175/JAMC-D-13-0182.1.

Bringi, V. N., and V. Chandrasekar, 2001: *Polarimetric Doppler Weather Radar: Principles and Applications*. Cambridge University Press, 636 pp.

——, T. D. Keenan, and V. Chandrasekar, 2001: Correcting C-band radar reflectivity and differential reflectivity data for rain attenuation: A self-consistent method with constraints. *IEEE Trans. Geosci. Remote Sens.*, **39**, 1906–1915, doi:10.1109/36.951081.

——, and Coauthors, 2006: Rainfall estimation from C-band polarimetric radar in Okinawa, Japan: Comparisons with 2D-video disdrometer and 400 MHz wind profiler. *J. Meteor. Soc. Japan*, **84**, 705–724, doi:10.2151/jmsj.84.705.

——, R. Thurai, and R. Hannesen, 2007: *Dual-Polarization Weather Radar Handbook.* 2nd ed. Gematronik GmbH, 163 pp.

——, C. R. Williams, M. Thurai, and P. T. May, 2009: Using dual-polarized radar and dual-frequency profiler for DSD characterization: A case study from Darwin, Australia. *J. Atmos. Oceanic Technol.*, **26**, 2107–2122, doi:10.1175/2009JTECHA1258.1.

——, M. Thurai, W. A. Petersen, and P. N. Gatlin, 2013: Using a network of 2D video disdrometers for external radar calibration of NASA's S-band polarimetric radar. *36th Conf. on Radar Meteorology*, Breckenridge, CO, Amer. Meteor. Soc., 10.3. [Available online at https://ams.confex.com/ams/36Radar/webprogram/Paper228161.html.]

——, L. Tolstoy, M. Thurai, and W. A. Petersen, 2015: Estimation of spatial correlation of drop size distribution parameters and rain rate using NASA's S-Band polarimetric radar and 2D video disdrometer network: Two case studies from MC3E. *J. Hydrometeor.*, **16**, 1207–1221, doi:10.1175/JHM-D-14-0204.1.

Chandrasekhar, V., L. Baldini, N. Bharadawaj, and P. L. Smith, 2014: Recommended calibration procedures for GPM ground validation radars. NASA Doc., 100 pp. [Available online at http://gpm-gv.gsfc.nasa.gov/Tier1/Docs/NASA_GPM_GV-cal_9.pdf.]

Chow, V. T., D. R. Maidment, and L. W. Mays, 1988: *Applied Hydrology.* McGraw-Hill, 570 pp.

Ciach, G. J., and W. F. Krajewski, 1999a: On the estimation of radar rainfall error variance. *Adv. Water Resour.*, **22**, 585–595, doi:10.1016/S0309-1708(98)00043-8.

——, and ——, 1999b: Radar–rain gauge comparisons under observational uncertainties. *J. Appl. Meteor.*, **38**, 1519–1525, doi:10.1175/1520-0450(1999)038<1519:RRGCUO>2.0.CO;2.

Cremonini, R., L. Baldini, E. Gorgucci, V. Romaniello, R. Bechini, and V. Campana, 2010: Observations of precipitation with X-band and C-band polarimetric radars in Piedmont region (Italy). *Proc. Sixth European Conf. on Radar in Meteorology and Hydrology*, Sibiu, Romania, Administratia Nationala de Meteorologie, 7 pp.

Cunha, L. K., J. A. Smith, W. F. Krajewski, M. L. Baeck, and B.-C. Seo, 2015: NEXRAD NWS polarimetric precipitation product evaluation for IFloodS. *J. Hydrometeor.*, **16**, 1676–1699, doi:10.1175/JHM-D-14-0148.1.

D'Adderio, L. P., F. Porcù, and A. Tokay, 2015: Identification and analysis of collisional breakup in natural rain. *J. Atmos. Sci.*, **72**, 3404–3416, doi:10.1175/JAS-D-14-0304.1.

Delrieu, G., S. Serrar, E. Guardo, and J. D. Creutin, 1999: Rain measurement in hilly terrain with X-band weather radar systems: Accuracy of path-integrated attenuation estimates derived from mountain returns. *J. Atmos. Oceanic Technol.*, **16**, 405–416, doi:10.1175/1520-0426(1999)016<0405:RMIHTW>2.0.CO;2.

Demir, I., and Coauthors, 2015: Data-enabled field experiment planning, management, and research using cyberinfrastructure. *J. Hydrometeor.*, **16**, 1155–1170, doi:10.1175/JHM-D-14-0163.1.

Doviak, R. J., and D. S. Zrnić, 1993: *Doppler Radar and Weather Observations.* Dover Publications, 562 pp.

Draper, N. R., and H. Smith, 1998: *Applied Regression Analysis.* 3rd ed. John Wiley & Sons, 736 pp.

Fabry, F., G. L. Austin, and D. Tees, 1992: The accuracy of rainfall estimates by radar as a function of range. *Quart. J. Roy. Meteor. Soc.*, **118**, 435–453, doi:10.1002/qj.49711850503.

Fjørtoft, R., and A. Lopès, 2001: Estimation of the mean radar reflectivity from a finite number of correlated samples. *IEEE Trans. Geosci. Remote Sens.*, **39**, 196–199, doi:10.1109/36.898684.

Galvez, M. B., J. Colom, V. Chandrasekar, F. Junyent, S. Cruz-Pol, and R. Rodriguez, 2009: Salient features of the radar nodes in the Puerto Rico tropical weather testbed. *IEEE Geoscience and Remote Sensing Symp.*, Cape Town, South Africa, IEEE, 841–844, doi:10.1109/IGARSS.2009.5417900.

Gatlin, P., and Coauthors, 2015: Searching for large raindrops: A global summary of two-dimensional video disdrometer observations. *J. Appl. Meteor. Climatol.*, **54**, 1069–1089, doi:10.1175/JAMC-D-14-0089.1.

Gebremichael, M., and W. F. Krajewski, 2004: Characterization of the temporal sampling error in space–time-averaged rainfall estimates from satellites. *J. Geophys. Res.*, **109**, D11110, doi:10.1029/2004JD004509.

Gekat, F., P. Meischner, K. Friedrich, M. Hagen, J. Koistinen, D. B. Michelson, and A. Huuskonen, 2004: The state of weather radar operations, networks and products. *Weather Radar: Principles and Advanced Applications*, P. Meischner, Ed., Springer-Verlag, 1–35.

Gorgucci, E., and V. Chandrasekar, 2005: Evaluation of attenuation correction methodology for dual-polarization radars: Application to X-band systems. *J. Atmos. Oceanic Technol.*, **22**, 1195–1206, doi:10.1175/JTECH1763.1.

Habib, E., G. Lee, D. Kim, and G. J. Ciach, 2010: Ground-based direct measurement. *Rainfall: State of the Science, Geophys. Monogr.*, Vol. 191, Amer. Geophys. Union, 61–77.

Hou, A. Y., G. Skofronick-Jackson, C. D. Kummerow, and J. M. Shepherd, 2008: Global precipitation measurement. *Precipitation: Advances in Measurement, Estimation and Prediction*, S. C. Michaelides, Ed., Springer, 131–169.

Huang, G.-J., V. N. Bringi, and M. Thurai, 2008: Orientation angle distributions of drops after an 80-m fall using a 2D video disdrometer. *J. Atmos. Oceanic Technol.*, **25**, 1717–1723, doi:10.1175/2008JTECHA1075.1.

Hubbert, J., and V. N. Bringi, 1995: An iterative filtering technique for the analysis of copolar differential phase and dual-frequency radar measurements. *J. Atmos. Oceanic Technol.*, **12**, 643–648, doi:10.1175/1520-0426(1995)012<0643:AIFTFT>2.0.CO;2.

Kabeche, F., J. Figueras i Ventura, B. Fradon, R. Hogan, A.-A. Boumahmoud, A. Illingworth, and P. Tabary, 2010: Towards X-band polarimetric quantitative precipitation estimation in mountainous regions: The RHYTMME project. *Proc. Sixth European Conf. on Radar in Meteorology and Hydrology*, Sibiu, Romania, Administratia Nationala de Meteorologie, 15 pp.

Kim, D.-S., M. Maki, and D.-I. Lee, 2010: Retrieval of three-dimensional raindrop size distribution using X-band polarimetric radar data. *J. Atmos. Oceanic Technol.*, **27**, 1265–1285, doi:10.1175/2010JTECHA1407.1.

Klazura, G. E., and D. A. Imy, 1993: A description of the initial set of analysis products available from the NEXRAD WSR-88D system. *Bull. Amer. Meteor. Soc.*, **74**, 1293–1311, doi:10.1175/1520-0477(1993)074<1293:ADOTIS>2.0.CO;2.

Krajewski, W. F., 2007: Ground networks: Are we doing the right thing? *Measuring Precipitation from Space: EURAINSAT and the Future*, V. Levizzani, P. Bauer, and F. J. Turk, Eds., Springer, 403–418.

——, and J. A. Smith, 2002: Radar hydrology: Rainfall estimation. *Adv. Water Resour.*, **25**, 1387–1394, doi:10.1016/S0309-1708(02)00062-3.

——, E. N. Anagnostou, and G. J. Ciach, 1996: Effects of the radar observation process on inferred rainfall statistics. *J. Geophys. Res.*, **101**, 26 493–26 502, doi:10.1029/96JD01616.

——, G. J. Ciach, and E. Habib, 2003: An analysis of small scale rainfall variability in different climatological regimes. *Hydrol. Sci. J.*, **48**, 151–162, doi:10.1623/hysj.48.2.151.44694.

——, G. Villarini, and J. A. Smith, 2010: Radar-rainfall uncertainties: Where are we after thirty years of effort? *Bull. Amer. Meteor. Soc.*, **91**, 87–94, doi:10.1175/2009BAMS2747.1.

Lapczak, S., and Coauthors, 1999: The Canadian national radar project. Preprints, *29th Conf. on Radar Meteorology*, Montreal, Canada, Amer. Meteor. Soc., 327–330.

Lin, Y., and K. E. Mitchell, 2005: The NCEP stage II/IV hourly precipitation analyses: development and applications. *19th Conf. on Hydrology*, San Diego, CA, Amer. Meteor. Soc., 1.2. [Available online at https://ams.confex.com/ams/Annual2005/techprogram/paper_83847.htm.]

Maki, M., and Coauthors, 2010: X-band polarimetric radar networks in urban areas. *Proc. Sixth European Conf. on Radar in Meteorology and Hydrology*, Sibiu, Romania, Administratia Nationala de Meteorologie, 202–206.

Matrosov, S. Y., D. E. Kingsmill, B. E. Martner, and F. M. Ralph, 2005: The utility of X-band polarimetric radar for quantitative estimates of rainfall parameters. *J. Hydrometeor.*, **6**, 248–262, doi:10.1175/JHM424.1.

McLaughlin, D., and Coauthors, 2009: Short-wavelength technology and the potential for distributed networks of small radar systems. *Bull. Amer. Meteor. Soc.*, **90**, 1797–1817, doi:10.1175/2009BAMS2507.1.

Mishra, K. V., 2012: Frequency diversity wideband digital receiver and signal processor for solid-state dual-polarimetric weather radars. M.S. thesis, Dept. of Electrical Engineering, Colorado State University, 158 pp.

——, A. Kruger, and W. F. Krajewski, 2013: Monitoring cross-channel correlation solar scan measurements using the Iowa X-band polarimetric radars. *Proc. IEEE Int. Geoscience and Remote Sensing Symp.*, Melbourne, Australia, IEEE, 1688–1691, doi:10.1109/IGARSS.2013.6723119.

Papoulis, A., and S. U. Pillai, 2002: *Probability, Random Variables and Stochastic Processes*. 4th ed. McGraw-Hill, 852 pp.

Park, S.-G., V. N. Bringi, V. Chandrasekar, M. Maki, and K. Iwanami, 2005a: Correction of radar reflectivity and differential reflectivity for rain attenuation at X band. Part I: Theoretical and empirical basis. *J. Atmos. Oceanic Technol.*, **22**, 1621–1632, doi:10.1175/JTECH1803.1.

——, M. Maki, K. Iwanami, V. N. Bringi, and V. Chandrasekar, 2005b: Correction of radar reflectivity and differential reflectivity for rain attenuation at X band. Part II: Evaluation and application. *J. Atmos. Oceanic Technol.*, **22**, 1633–1655, doi:10.1175/JTECH1804.1.

Pazmany, A. L., J. B. Mead, H. B. Bluestein, J. C. Snyder, and J. B. Houser, 2013: A mobile rapid-scanning X-band polarimetric (RaXPol) Doppler radar system. *J. Atmos. Oceanic Technol.*, **30**, 1398–1413, doi:10.1175/JTECH-D-12-00166.1.

Petersen, W., and W. F. Krajewski, 2013: Status update on the GPM Ground Validation Iowa Flood Studies (IFloodS) field experiment. *Geophysical Research Abstracts*, Vol. 15, Abstract 13345. [Available online at http://meetingorganizer.copernicus.org/EGU2013/EGU2013-13345.pdf.]

Picciotti, E., and Coauthors, 2013: Coupling X-band dual-polarized mini-radars and hydro-meteorological forecast models: The HYDRORAD project. *Nat. Hazards Earth Syst. Sci.*, **13**, 1229–1241, doi:10.5194/nhess-13-1229-2013.

Purdy, J. C., G. L. Austin, A. W. Seed, and I. D. Cluckie, 2005: Radar evidence of orographic enhancement due to the seeder feeder mechanism. *Meteor. Appl.*, **12**, 199–206, doi:10.1017/S1350482705001672.

Ryzhkov, A., S. E. Giangrande, and T. J. Schuur, 2005: Rainfall estimation with a polarimetric prototype of WSR-88D. *J. Appl. Meteor.*, **44**, 502–515, doi:10.1175/JAM2213.1.

——, M. Diederich, P. Zhang, and C. Simmer, 2014: Potential utilization of specific attenuation for rainfall estimation, mitigation of partial beam blockage, and radar networking. *J. Atmos. Oceanic Technol.*, **31**, 599–619, doi:10.1175/JTECH-D-13-00038.1.

Scherier, P. J., and L. L. Scharf, 2010: *Statistical Signal Processing of Complex-Valued Data: The Theory of Improper and Noncircular Signals*. Cambridge University Press, 330 pp.

Schneebeli, M., N. Dawes, M. Lehning, and A. Berne, 2013: High-resolution vertical profiles of X-band polarimetric radar observables during snowfall in the Swiss Alps. *J. Appl. Meteor. Climatol.*, **52**, 378–394, doi:10.1175/JAMC-D-12-015.1.

Scipión, D. E., R. Mott, M. Lehning, M. Schneebeli, and A. Berne, 2013: Seasonal small-scale spatial variability in alpine snowfall and snow accumulation. *Water Resour. Res.*, **49**, 1446–1457, doi:10.1002/wrcr.20135.

Seo, B.-C., B. Dolan, W. F. Krajewski, S. A. Rutledge, and W. Petersen, 2015: Comparison of NEXRAD single and dual polarization based rainfall estimates for the NASA Iowa Flood Studies project. *J. Hydrometeor.*, **16**, 1658–1675, doi:10.1175/JHM-D-14-0169.1.

Seo, D. J., and J. A. Smith, 1996: Characterization of the climatological variability of mean areal rainfall through fractional coverage. *Water Resour. Res.*, **32**, 2087–2095, doi:10.1029/96WR00486.

Smith, J. A., D. J. Seo, M. L. Baeck, and M. D. Hudlow, 1996: An intercomparison study of NEXRAD precipitation estimates. *Water Resour. Res.*, **32**, 2035–2045, doi:10.1029/96WR00270.

Smyth, T. J., and A. J. Illingworth, 1998: Correction for attenuation of radar reflectivity using polarization data. *Quart. J. Roy. Meteor. Soc.*, **124**, 2393–2415, doi:10.1002/qj.49712455111.

Tabary, P., 2007: The new French operational radar rainfall product. Part I: Methodology. *Wea. Forecasting*, **22**, 393–408, doi:10.1175/WAF1004.1.

——, G. Vulpiani, J. J. Gourley, A. J. Illingworth, R. J. Thompson, and O. Bousquet, 2009: Unusually high differential attenuation at C Band: Results from a two-year analysis of the French Trappes polarimetric radar data. *J. Appl. Meteor. Climatol.*, **48**, 2037–2053, doi:10.1175/2009JAMC2039.1.

Testud, J., E. Le Bouar, E. Obligis, and M. Ali-Mehenni, 2000: The rain profiling algorithm applied to polarimetric weather radar. *J. Atmos. Oceanic Technol.*, **17**, 332–356, doi:10.1175/1520-0426(2000)017<0332:TRPAAT>2.0.CO;2.

Thurai, M., G.-J. Huang, V. N. Bringi, W. L. Randeu, and M. M. Schönhuber, 2007: Drop shapes, model comparisons, and calculations of polarimetric radar parameters in rain. *J. Atmos. Oceanic Technol.*, **24**, 1019–1032, doi:10.1175/JTECH2051.1.

——, W. A. Petersen, P. Gatlin, V. N. Bringi, D. B. Wolff, and D. A. Marks, 2013: Absolute calibration of NASA's S-band polarimetric radar (NPOL) during IFloodS campaign using 2D video disdrometers (2DVD). *2013 Fall Meeting*, San Francisco, CA, Amer. Geophys. Union, Abstract H33E-1389.

Torres, S., and D. S. Zrnić, 2003: Whitening of signals in range to improve estimates of polarimetric variables. *J. Atmos. Oceanic Technol.*, **20**, 1776–1789, doi:10.1175/1520-0426(2003)020<1776:WOSIRT>2.0.CO;2.

Uijlenhoet, R., and A. Berne, 2008: Stochastic simulation experiment to assess radar rainfall retrieval uncertainties associated with attenuation and its correction. *Hydrol. Earth Syst. Sci.*, **12**, 587–601, doi:10.5194/hess-12-587-2008.

van de Beek, C. Z., H. Leijnse, J. N. M. Stricker, R. Uijlenhoet, and H. W. J. Russchenberg, 2010: Performance of high-resolution X-band radar for rainfall measurement in the Netherlands. *Hydrol. Earth Syst. Sci.*, **14**, 205–221, doi:10.5194/hess-14-205-2010.

Villarini, G., and W. F. Krajewski, 2010: Review of the different sources of uncertainty in single polarization radar-based estimates of rainfall. *Surv. Geophys.*, **31**, 107–129, doi:10.1007/s10712-009-9079-x.

Wilson, J. W., and E. A. Brandes, 1979: Radar measurement of rainfall—A summary. *Bull. Amer. Meteor. Soc.*, **60**, 1048–1058, doi:10.1175/1520-0477(1979)060<1048:RMORS>2.0.CO;2.

Yoshikawa, E., and Coauthors, 2010: Development and initial observation of high-resolution volume-scanning radar for meteorological application. *IEEE Trans. Geosci. Remote Sens.*, **48**, 3225–3235, doi:10.1109/TGRS.2010.2045762.

Zawadzki, I., 1982: The quantitative interpretation of weather radar measurements. *Atmos.–Ocean*, **20**, 158–180, doi:10.1080/07055900.1982.9649137.

Zhang, J., and Coauthors, 2011: National mosaic and multi-sensor QPE (NMQ) system: Description, results, and future plans. *Bull. Amer. Meteor. Soc.*, **92**, 1321–1338, doi:10.1175/2011BAMS-D-11-00047.1.

Zrnić, D., and P. Mahapatra, 1985: Two methods of ambiguity resolution in pulsed Doppler weather radars. *IEEE Trans. Aerosp. Electron. Syst.*, **AES-21**, 470–483, doi:10.1109/TAES.1985.310635.